Resource

SOURCE DATA | TRANSPARENT PROCESS | OPEN ACCESS | CHECK FOR UPDATES

EMBO reports

Proximity proteomics reveals a co-evolved LRRK2-regulatory network linked to centrosomes

Marita Eckert [1,2,5], Pasquale Miglionico [3,5], Francesca Izzi[1], Natalia De Oliveira Rosa [3], Benjamin Riebenbauer[1], Marius Ueffing [4], Francesco Raimondi [3]✉ & Christian Johannes Gloeckner [1,4]✉

Abstract

Leucine-rich repeat kinase 2 (LRRK2) not only plays a vital role in familial forms of Parkinson's disease (PD) but also represents a risk factor for idiopathic PD. Its multi-domain architecture enables fine-tuned regulation of its biological function by orchestrating intra- and inter-molecular interactions. Here, we present BioID proximity proteomes of LRRK2 that reveal new interactors, which we further characterize using a novel evolutionary and structural bioinformatics pipeline. Co-evolutionary analysis of the protein–protein interaction network identifies a structural and functional module enriched in cytoskeletal components associated with the centrosome and microtubules. In addition, structural modeling of binary interactions using AlphaFold-Multimer reveals distinct groups of interactors that engage LRRK2 in a manner dependent on specific conformations and epitopes. Furthermore, we identify distinct changes in the LRRK2 proximity proteome that are induced by the type I kinase inhibitor MLi-2 or by co-expression of the LRRK2 upstream effector RAB29. Depending on its activity state and conformation, these protein–protein interactions link LRRK2 to defined cellular sub-compartments, including centriolar satellites and vesicular sub-compartments.

Subject Categories Cell Adhesion, Polarity & Cytoskeleton; Methods & Resources; Signal Transduction
https://doi.org/10.1038/s44319-026-00806-4
Received 10 October 2024; Revised 1 April 2026;
Accepted 29 April 2026
Published online: 23 May 2026

Introduction

Parkinson's disease (PD) is the second most common neurodegenerative disease after Alzheimer's. It occurs mostly sporadically and is distributed with high frequency in the older generations. PD is characterized by a loss of dopaminergic neurons in the *substantia nigra*, leading to the motor symptoms associated with the disease (Fahn, 2003). Several therapies targeting the symptoms, such as dopamine substitution, are used; however, no causative therapy currently exists. About 5–10% of PD cases are hereditary (Gasser et al, 2011). *LRRK2*, localized within the PARK8 locus and coding for the Leucine-rich repeat kinase 2, is one of the genes associated with familial forms of the disease but also represents a risk factor in idiopathic PD (Paisan-Ruiz et al, 2004; Simon-Sanchez et al, 2009; Zimprich et al, 2004). The multi-domain protein LRRK2 is an active protein kinase and, at least, mutations with confirmed disease segregation, including the most common G2019S variant within its kinase domain, augment its kinase activity (Kalogeropulou et al, 2022). This makes LRRK2 an important drug target (Kluss et al, 2022b). ATP-competitive LRRK2-specific kinase inhibitors for PD-treatment are under development and in clinical trials (Jennings et al, 2022). Nevertheless, structural changes of the lung observed in non-human primates indicate a relatively small therapeutic window and additionally challenge a long-term treatment with these compounds necessary to allow a lifelong reduction of augmented LRRK2 pathway activation (Miller et al, 2023). For this reason, the identification of alternative drug targets within the LRRK2-associated pathways would be a potential solution for better control of pathophysiological alterations associated with pathogenic forms of this protein, minimizing the risk of drug-induced lung pathologies. In addition, a larger group of patients beyond LRRK2 mutation carriers might benefit from targeting more common PD-associated pathways.

Various studies have demonstrated that LRRK2 functions in vesicle trafficking, including presynaptic vesicles as well as autophagy and lysosomal pathways (Piccoli et al, 2011; reviewed in: Follett and Farrer, 2021). In agreement with these cellular functions, LRRK2 phosphorylates a subset of Rab proteins, small G-proteins involved in vesicular transport, such as RAB8A and RAB10, which are elevated by PD-associated LRRK2 variants (Steger et al, 2017).

In common with other Roco proteins, LRRK2 features a remarkable complexity (Wauters et al, 2019). In fact, LRRK2 contains multiple scaffolding domains, not only involved in maintaining LRRK2 in an auto-inhibited state, as recently demonstrated by high-resolution structures of LRRK2 (Deniston et al, 2020; Myasnikov et al, 2021), but also in mediating protein–protein interactions, making LRRK2 a signaling hub possibly integrating multiple up- and downstream signals (reviewed in: Manzoni et al, 2015). These studies

[1]German Center for Neurodegenerative Diseases, Tübingen, Germany. [2]Graduate School of Cellular and Molecular Neuroscience, University of Tübingen, Tübingen, Germany. [3]Laboratorio di Biologia Bio@SNS Scuola Normale Superiore, Pisa, Italy. [4]Center for Ophthalmology, Institute for Ophthalmic Research, University of Tübingen, Tübingen, Germany. [5]These authors contributed equally: Marita Eckert, Pasquale Miglionico. ✉E-mail: francesco.raimondi@sns.it; johannes.gloeckner@dzne.de

suggest that the Roco protein LRRK2 is a tightly controlled protein kinase serving as hub and signal integrator and is most likely involved in context-specific, spatially controlled cellular responses that appear evolutionarily conserved. Considerable effort has therefore been spent on the investigation of the protein–protein interaction networks of LRRK2, mainly using affinity-based methods. Various studies have investigated the LRRK2 interactome across different cellular contexts and model organisms (Islam et al, 2016; Meixner et al, 2011; Piccoli et al, 2011; Piccoli et al, 2014). These data have been curated in public databases such as IntAct or STRING and subjected to meta-analysis to dissect functional LRRK2 signaling networks (Gloeckner and Porras, 2020; Manzoni et al, 2015; Zhao et al, 2024; Zhao et al, 2023). However, most approaches rely on immunoprecipitation or pull-down methods, which are biased toward stable complexes and may underrepresent transient interactions.

To overcome these limitations, we applied the BioID proximity labeling approach to identify LRRK2 interaction partners in living cells. Using BioID with three different tags, we define the proximity proteome of LRRK2 under basal conditions. In addition, using a newly designed bioinformatics workflow that estimates co-evolution of interacting partners based on their co-occurrence across sequenced genomes, we show that the resulting BioID datasets are enriched for interactions with high co-evolution scores, comparable to confirmed direct interactions. This approach identifies a cluster of interactors with strong co-evolution to LRRK2, enriched in cytoskeletal proteins associated with centrosomal and ciliary dynamics. Furthermore, structural modeling of binary complexes using AlphaFold-Multimer reveals distinct conformations and interaction interfaces linked to specific functional processes. Finally, to further stratify the LRRK2 interactome, we analyzed experimentally defined conformational states, including co-expression with the upstream effector RAB29 and stabilization of an active-like kinase conformation by a type I inhibitor (Taylor et al, 2020; Wauters et al, 2019). Notably, MLi-2, but not GZD-824, enriched a specific sub-interactome associated with centriolar satellites.

Results

Definition of cellular LRRK2 proximity proteomes with BioID1, BioID2 and miniTurbo

To characterize the LRRK2 interactome, we applied the proximity labeling approach BioID, which enables the identification of protein–protein interactions in living cells, including transient interactions. To define the LRRK2 proximity proteome, we generated N-terminal fusion constructs using the original BioID (BioID1), BioID2, and miniTurbo tags.

All constructs were functionally validated to confirm biotinylation activity and to ensure that the tags did not interfere with LRRK2 function. Western blot analysis demonstrated efficient biotinylation for all constructs (Appendix Fig. S1), with BioID2 and miniTurbo showing higher labeling efficiency compared to BioID1. We further confirmed that the fusion proteins retained kinase activity by assessing phosphorylation of the physiological LRRK2 substrate Rab10 at Thr73 (Appendix Fig. S1).

Following validation, all three constructs were used to determine their interactomes upon transient expression in HEK293T cells. To increase stringency, a tag-only control was used as a reference. For relative comparisons, expression levels were adjusted in preliminary experiments and consistently verified by Western blot analysis of cell lysates. The use of a tag-only control enabled the efficient exclusion of endogenously biotinylated proteins, whose labeling is inherently increased by biotin supplementation.

Data from all three proximity proteomes were analyzed using SAINTexpress and, independently, by label-free quantification (LFQ) combined with an FDR-controlled *t* test implemented in Perseus (Tyanova et al, 2016). To further refine the dataset, we applied a bioinformatics pipeline incorporating co-evolution analysis of interacting proteins and structural modeling using AlphaFold-Multimer (Fig. 1A).

Using LFQ, 168, 312, and 241 proteins were identified as significantly enriched in the LRRK2 condition compared to the tag-only control for BioID1, BioID2, and miniTurbo, respectively (Fig. 1B; Dataset EV1). SAINTexpress (Teo et al, 2014), followed by filtering against the CRAPome database (Mellacheruvu et al, 2013), provided a more stringent set compared to LFQ-based analysis. Based on this approach, we defined a non-redundant set of 208 unique interactors, hereafter referred to as the "BioID set," which was subjected to downstream bioinformatics analysis.

Functional-enrichment analysis of the LRRK2 proximity proteome

We compared the LRRK2 BioID interactome with a reference LRRK2 interactome available from IntAct (Orchard et al, 2014). We found that only 54 interactors in the filtered BioID set were previously reported to be associated with LRRK2, whereas the majority (154) have not been reported before (Fig. 2A,B). By integrating the LRRK2 BioID interactome with known interactions from IntAct, we defined modules of proteins that interact not only with LRRK2 but also with each other, thereby revealing structured interaction networks (Fig. 2A). Among the enriched intracellular and cytosolic compartments, we found terms related to microtubules (e.g., Microtubule Cytoskeleton, FDR = 5.83E-15) and Centrosome (FDR = 1.43E-13), emphasizing the importance of LRRK2 in microtubule organization (Fig. 2C), and representing the largest module of interacting proteins in the network (Fig. 2A). In addition, we also found processes related to cell cycle and mitosis (e.g., "Regulation of mitotic cell cycle", FDR = 9.71E-08) (Fig. 2D).

Multiple protein domains instances are significantly enriched within the list of identified LRRK2 interaction partners (Fig. 2E). In particular, we found that the Armadillo-type fold instance is the most enriched one (FDR = 9.58E-06), which is found in 21 distinct interactors, followed by other domains with lower, but still significant, degree of enrichment, such as "Forkhead-associated (FHA) domain" (Almawi et al, 2017), found in six distinct proteins, the "DIX domain" (Ehebauer and Arias, 2009; Kafka et al, 2014) found in four proteins, the "K Homology domain, type 1" (Grishin, 2001) found in six proteins and "Ubiquitin-like domain superfamily" (FDR < 0.05), the latter being found in 11 distinct interacting proteins. Interestingly, LRRK2 and its Drosophila orthologue dLRRK have been demonstrated to functionally interact with the Forkhead box transcription factor FoxO1/dFoxO. In particular, LRRK2-mediated phosphorylation of FoxO1 enhances its transcriptional activity, leading to neuronal toxicity (Kanao et al, 2010).

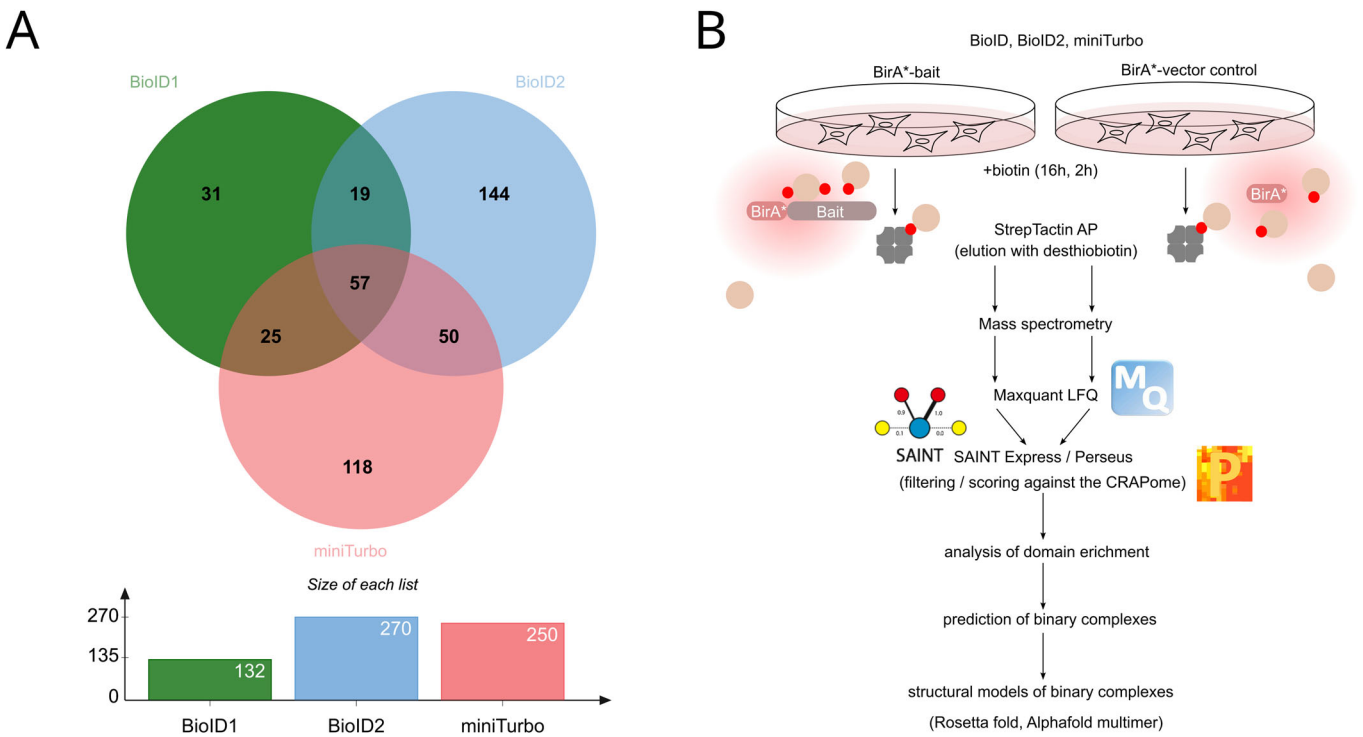

Figure 1. Workflow and overview of the LRRK2 BioID proximity proteome analysis.

(**A**) Workflow of the BioID analysis and post processing of the data. (**B**) Overlap between the different BioID approaches. Enriched proteins were determined by relative label-free quantification (combined with an FDR-controlled *T* test, $P = 0.05$) of BioID LRRK2 vs the corresponding tag-only control: BioID1-LRRK2/BioID1-tag: $N = 8$, BioID2-LRRK2/BioID2: $N = 9$, miniTurbo-LRRK2/miniTurbo tag: $N = 8$.

A cluster of proteins involved in centrosome/microtubular dynamics is most co-evolved with LRRK2

We analyzed the extent of co-evolution between LRRK2 and its interactors to prioritize the most conserved relationships associated with LRRK2's functions. We derived a metric for the co-evolution between two interacting proteins based on the degree of co-presence, assessed through a Jaccard score, of interacting gene pairs in sequenced genomes available from a reference orthology database (e.g., OMA, see "Methods"). We found that this simple co-evolutionary metric is informative for identifying non-enzymatic, direct interactions as well as stable complexes at the level of the human interactome (Meldal et al, 2022; Miglionico et al, 2024; Orchard et al, 2014) (Dataset EV2A). We observed similar trends when focusing on LRRK2 interactions reported in IntAct, with "non-enzymatic direct" PPIs being characterized by a significantly higher Jaccard score compared to those categorized as "association" or "physical interaction" (Fig. 3A). Intriguingly, we found that the distribution of co-evolution metrics calculated for BioID interactors is significantly higher than most IntAct categories (i.e., "association", "physical", "enzymatic direct") and it is as high as the non-enzymatic direct interactions (Fig. 3A). This result suggests that interactors captured within the BioID dataset may represent stable, direct interaction partners of LRRK2 with whom they co-evolved. Likewise, simple co-evolution scores are predictive for LRRK2 direct interactions, particularly the non-enzymatic direct ones (Fig. 3B; ROC AUC = 0.715). In the case of the LRRK2 interactome, we found that this co-evolutionary metric is more predictive of non-enzymatic direct interaction compared to another co-evolution estimate, i.e., Mutual Information (ROC AUC = 0.66; Appendix Fig. S2), which is instead more predictive at a human proteome scale (Miglionico et al, 2024).

We used the co-evolution metric to cluster LRRK2 and its interactors, which revealed groups of proteins characterized by reciprocal high co-evolution (Fig. 3C). The different groups of interactors are also characterized by specific biological processes, which are overall mutually exclusive to each other, suggesting that clusters of co-evolved proteins underpin specific functional interactions and biological processes (Appendix Fig. S3). Notably, the cluster containing LRRK2 (i.e., Cluster 2) is characterized by on average higher co-evolution and several highly co-evolved proteins (Fig. 3C). The top ten proteins of Cluster 2 showing the highest co-evolution are summarized in Table 1. By mapping members of this cluster onto the STRING functional interaction network (Fig. 3D, see "Methods"), we found functional interactions for most of the members, including LRRK2. Overall, STRING yielded a highly significant PPI enrichment ($P = 1.0E-16$), suggesting that these proteins are more likely to interact with themselves than with randomly selected proteins. Moreover, network topology analysis delineated two distinct submodules: the first encompassing LRRK2 together with proteins predominantly linked to Wnt signaling (FDR = 0.0013; Fig. 3E), and the second consisting of proteins implicated in cytoskeletal processes ("Protein localization to microtubule cytoskeleton"; FDR = 2.18E-05), centrosome dynamics ("Loss of Nlp from mitotic centrosomes"; FDR = 0.00086) and centriole organization ("Centriole"; FDR = 1.11E-05). Consistently, Cluster 2 displayed strong enrichment for cellular component

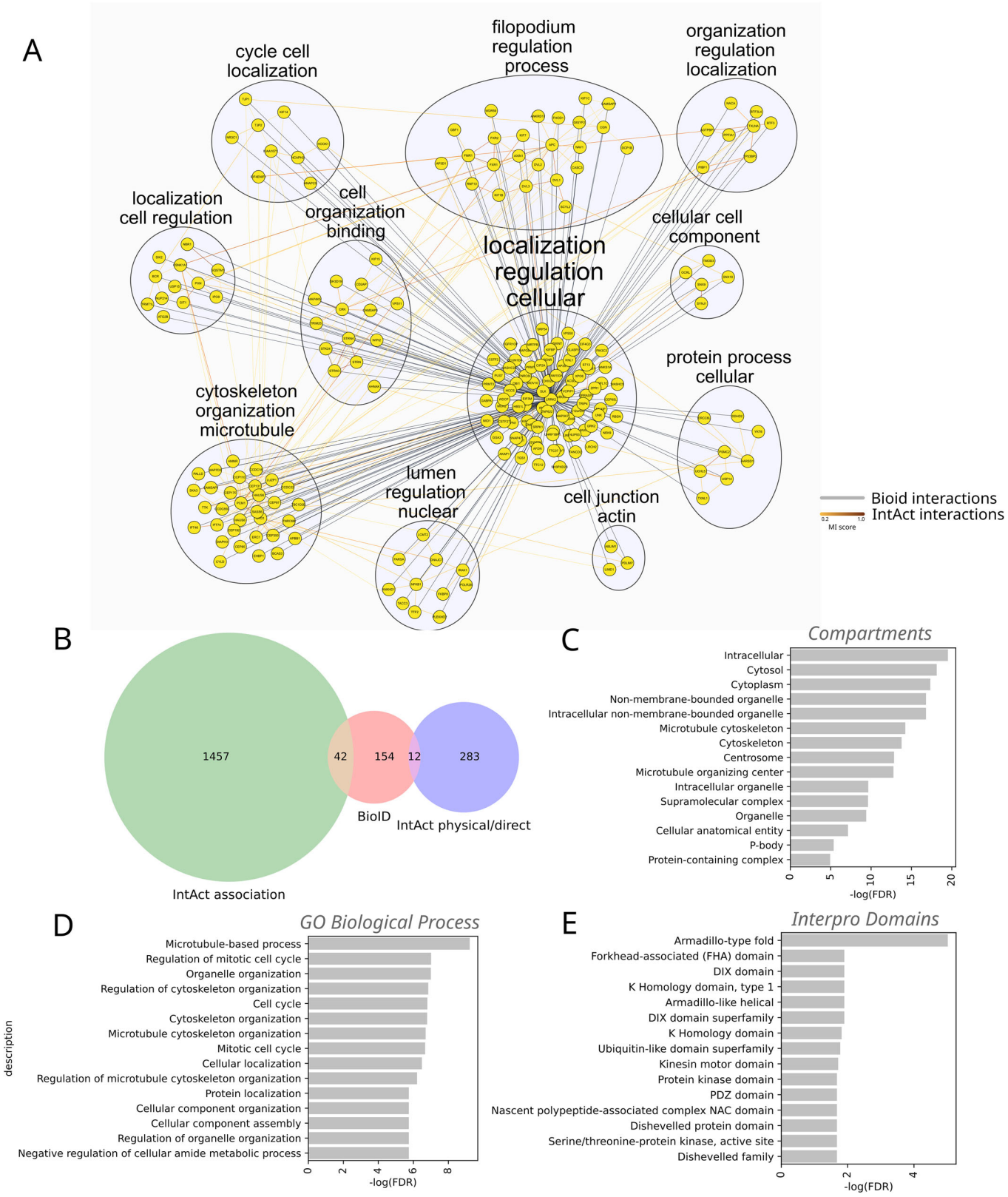
A
cycle cell localization
filopodium regulation process
organization regulation localization
localization cell regulation
cell organization binding
localization regulation cellular
cellular cell component
protein process cellular
cytoskeleton organization microtubule
lumen regulation nuclear
cell junction actin
Bioid interactions
IntAct interactions
MI score
B
1457
42
154
12
283
BioID
IntAct physical/direct
IntAct association
C
Compartments
Intracellular
Cytosol
Cytoplasm
Non-membrane-bounded organelle
Intracellular non-membrane-bounded organelle
Microtubule cytoskeleton
Cytoskeleton
Centrosome
Microtubule organizing center
Intracellular organelle
Supramolecular complex
Organelle
Cellular anatomical entity
P-body
Protein-containing complex
-log(FDR)
D
GO Biological Process
description
Microtubule-based process
Regulation of mitotic cell cycle
Organelle organization
Regulation of cytoskeleton organization
Cell cycle
Cytoskeleton organization
Microtubule cytoskeleton organization
Mitotic cell cycle
Cellular localization
Regulation of microtubule cytoskeleton organization
Protein localization
Cellular component organization
Cellular component assembly
Regulation of organelle organization
Negative regulation of cellular amide metabolic process
-log(FDR)
E
Interpro Domains
Armadillo-type fold
Forkhead-associated (FHA) domain
DIX domain
K Homology domain, type 1
Armadillo-like helical
DIX domain superfamily
K Homology domain
Ubiquitin-like domain superfamily
Kinesin motor domain
Protein kinase domain
PDZ domain
Nascent polypeptide-associated complex NAC domain
Dishevelled protein domain
Serine/threonine-protein kinase, active site
Dishevelled family
-log(FDR)

Figure 2. LRRK2 interactome functional enrichment.

(A) The LRRK2 BioID interaction network was mapped on known PPIs from IntAct via Cytoscape. The edges' color and thickness for mapped interactions are proportional to IntAct MI score, else they are colored in gray with constant thickness. Modules within the network have been identified through the Glay method of the Autoannotate app, and nodes colored accordingly. Labels were calculated using the 'Adjacent Words' setting of the WordCloud algorithm, based on significantly enriched (FDR < 0.01) Gene Ontology (GO) Biological Processes and Cellular Component terms associated with each gene in the network. **(B)** Venn diagram showing the overlap between the BioID interaction sets and known LRRK2 interactions in IntAct; barplots showing the top 15 most significant terms obtained through String's functional enrichment of **(C)** Compartments, **(D)** GO Biological Process, and **(E)** Interpro domains.

terms, most notably "Microtubule Cytoskeleton" (FDR = 2.10E-12) and "Centrosome" (FDR = 1.01E-12) (Dataset EV2B). Interestingly, CYLD is the most co-evolved protein of LRRK2, a deubiquitinase that acts as a negative regulator of dopamine neuron survival in Parkinson's disease (Pirooznia et al, 2022) but has not yet been reported to directly interact with LRRK2. Notably, CYLD emerges as a critical bridging element that connects the two principal submodules within Cluster 2's interactome (Fig. 3D).

On the other hand, Cluster 1 is characterized by distinct processes, such as FAR/SIN/STRIPAK complex ($P = 0.0012$; Dataset EV2B). Taken together, these results suggest that our co-evolution-based approach was able to identify a group of LRRK2-interacting proteins, mostly associated with microtubule and centrosome functions via the formation of stable, supramolecular complexes.

Likewise, co-evolution-based clustering of LRRK2 interactors from IntAct shows interactors such as RAB29, RAB12, LRRK1, or SNCA among the most co-evolved partners that cluster with LRRK2 (Appendix Fig. S4), confirming the tight evolutionary constraint on LRRK2's functional regulation.

After validating CYLD as part of the LRRK2 proximity proteome by Western blot analysis (Fig. 3F), we investigated the functional relevance of this association by assessing whether CYLD influences LRRK2 abundance. To this end, LRRK2 wild-type or the pathogenic Y1699C variant was co-expressed with CYLD or an empty vector control. Y1699C was chosen, as this variant shows a robust increase in Rab phosphorylation (Kalogeropulou et al, 2022) and reduced steady-state protein levels under our experimental conditions. As the classical ECL-based western blot did not allow reliable quantification of the large protein LRRK2 (286 kDa), we used a capillary-based western system with fluorescent detection.

CYLD co-expression was associated with increased steady-state LRRK2 levels across two independent experiments ($N = 6$ biological replicates each), with the effect being more pronounced for the Y1699C variant. Wild-type LRRK2 showed a smaller increase, consistent with a weaker trend (Fig. 3G; Appendix Fig. S5A).

Because CYLD preferentially acts on K63-linked chains, we repeated the experiment with additional co-expression of either wild-type ubiquitin or a K63-only ubiquitin mutant, which restricts linkage to lysine 63 (Lim et al, 2005). However, while replicating the effects seen without Ubiquitin overexpression, these data do not allow conclusions about the contribution of specific ubiquitin linkage types (Appendix Fig. S5B).

AF-based modeling reveals a discrete repertoire of conformations and interfaces shaping the LRRK2 interactome

We predicted 3D complexes for binary interactions of LRRK2 and 196 partners in the BioID dataset via AlphaFold-multimer (AF) and characterized their interfaces and conformations (Fig. 4A).

We structurally aligned LRRK2 conformations across different complexes by superimposing the monomeric LRRK2 chains and subsequently calculating the pairwise root-mean-square deviation (RMSD) for all possible pairs (Fig. 4A; "Methods"). We performed hierarchical clustering of LRRK2 structures based on RMSD, through which we identified two main clusters (Fig. 4B). A smaller one is characterized by conformations with lower deviation from the inactive LRRK2 structure (PDB ID: 7LHW), which we termed "locked" (Fig. 4B–D). The main structural hallmarks characterizing the "locked" conformation, which are inherited by the experimental inactive LRRK2 structure (PDB:7LHW) (Myasnikov et al, 2021), are the LRR wrapping around the catalytic domains, particularly the kinase, and a contact formed by the extended loop within the LRR repeats, which includes the hinge helix, and the C-terminal WD40 (Myasnikov et al, 2021). A larger cluster comprised conformations characterized by a greater deviation from the inactive structure due to major rearrangements of the LRR, ROC, and COR domains, which we termed "unlocked" (Fig. 4B–D). Such conformations are reminiscent of the ones that we observed in the predicted LRRK2-RAB10 complex, which we validated as the AF-predicted conformation best accommodating experimental XL-MS data (preprint: Guaitoli et al, 2023). Intriguingly, we found that proteins interacting with LRRK2 in these two alternative conformations are associated with distinct evolutionary and functional properties. Indeed, LRRK2 complexes in the "locked" conformations are characterized by significantly lower RMSD ($P = 3.81E-20$; Fig. 4D) and higher co-evolution ($P = 1.33E-3$; Fig. 4E) than complexes in the "unlocked" conformations. The two groups are also associated with largely distinct enriched processes (Fig. 4F).

In particular, the interactors engaging with LRRK2 in the locked conformation are significantly associated with processes linked to centriolar satellites ($P = 4.76E-10$) and cilium assembly ($P = 0.0001$) (Fig. 4G; Dataset EV2C). Those interacting with the unlocked conformations are associated with a higher number of enriched processes, including cluster-specific ones such as the cytoskeleton ($P = 4.53E-09$) or the microtubule-organizing center MTOC ($P = 6.40E-07$). Hence, the predicted LRRK2 conformational switch might be relevant in orchestrating the interaction with partners associated with distinct functions.

We also explored patterns of interactor engagement across the different regions of the LRRK2 multi-domain architecture. To this end, we considered the distribution of distance probabilities (i.e., distograms) generated by AF for each binary interaction and mapped the most likely interacting residues of the partners with respect to LRRK2 positions. We used these partner-specific interaction fingerprints to cluster the interactome and identified four major groups of proteins, each named according to the LRRK2 3D interface involved in the interaction (Fig. 5A; Dataset EV2D; see "Methods"). The Core cluster comprises partners that interact with the LRR–ROC–COR–KIN domains and was named accordingly, as these domains represent the most evolutionarily conserved regions of LRRK2 (Fig. 5A,B). The WD40 cluster includes complexes

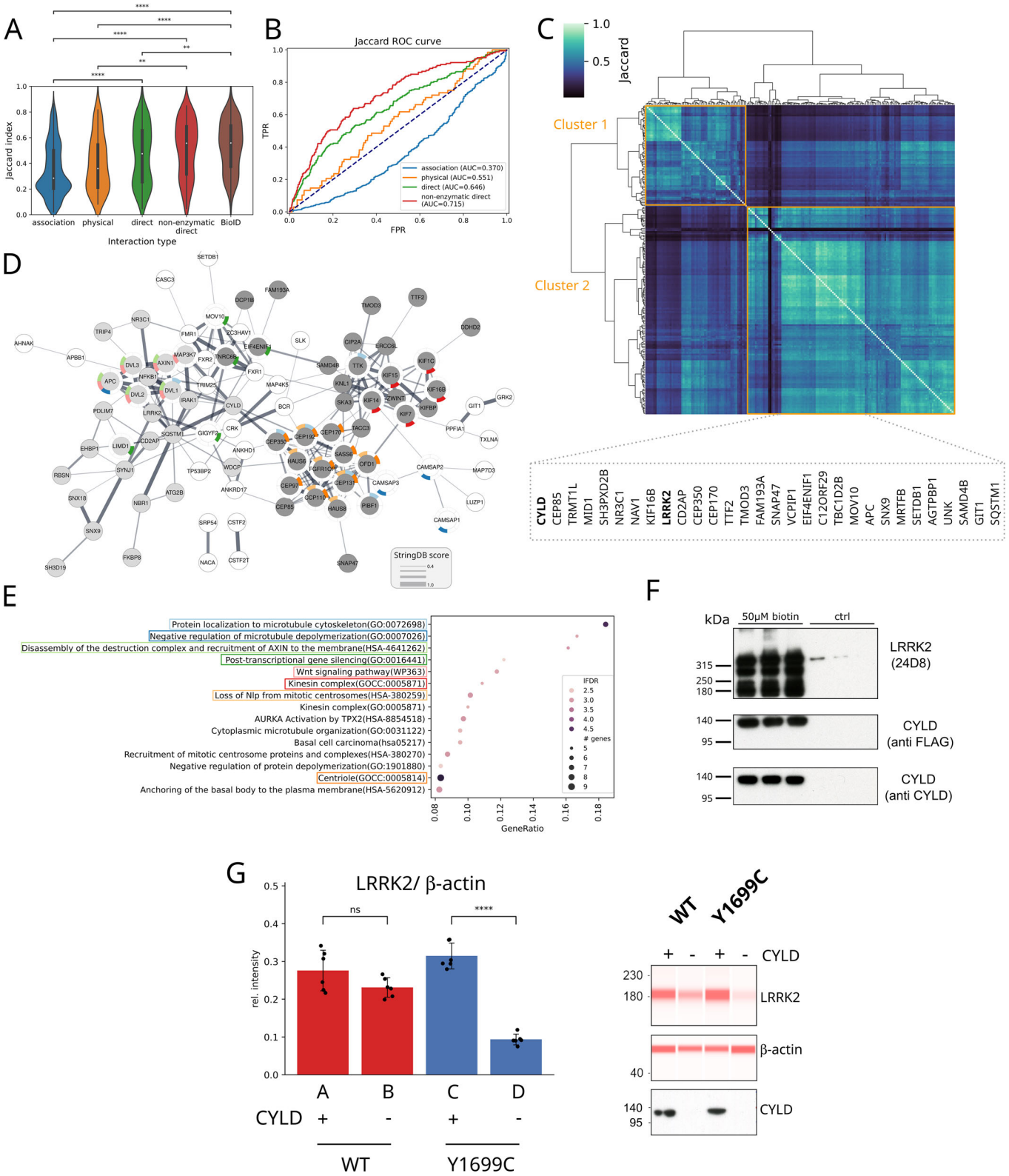

involving the homonymous domain (Fig. 5A,C), while the ARM cluster comprises proteins engaging with a newly identified site within the Armadillo domain (Fig. 5A,D). Lastly, the "Other" cluster contains proteins with alternative interaction modalities or no clearly defined binding interface (Fig. 5A). Complexes predicted to interact with the Core group displayed significantly higher AlphaFold confidence scores compared to those interacting with the WD40 domain ($P = 1.14E-8$) or via "Other" interaction modalities ($P = 4.86E-14$; Fig. 5E). Complexes of

Figure 3. Co-evolution analysis of LRRK2 interactome.

(**A**) Distribution of co-evolution metric (i.e., Jaccard score) among the different LRRK2 interaction sets, including IntAct interaction types and BIOID. *P* values have been computed with a two-sided Mann–Whitney test with Bonferroni correction (*P < 0.05, **P < 0.01, ***P < 0.001, ****P < 0.0001). The plot shows the comparison between 2062 independent samples divided into five classes with the following number of elements: association 1424, physical 68, direct 215, non-enzymatic direct 166, BioID 189. *P* values: association-direct: 1.2E-11; association-non-enzymatic direct: 5.8E-19; association-BioID: 6.1E-29; physical-non-enzymatic direct: 0.0017; physical-BioID: 2.7E-5; direct-BioID: 0.0082. Violin plots show the median as the white central dot and first and third quartiles as bounds of the thicker black line (box); the whiskers extend to the last data point within 1.5 times the interquartile range (IQR) from the box boundaries. (**B**) Predictiveness of LRRK2 interaction type via co-evolution. (**C**) Heatmap showing the hierarchical clustering based on the degree of co-evolution (Jaccard score) of the LRRK2 proximity proteome. (**D**) String network of the proteins most co-evolved with LRRK2 participating in cluster 2. Nodes are colored in gray or light gray according to module membership determined with the MCL approach available from the Cytoscape clusterMaker app. Node rims are colored according to enriched processes. (**E**) Dot plot showing top 15 significantly enriched (FDR < 0.01) categories from the string network of cluster 2. Values on the *x* axis display the ratio of genes of the term participating to the network over the total number of genes in that category. The size of the dot is proportional to the number of genes of that category in the network, while the node color is the darker the more significant is the category enrichment. Only categories with at least five genes have been displayed. Representative, enriched categories have been colored with the same color scheme as in (**D**). (**F**) Validation of CYLD as part of the LRRK2 proximity proteome by Western blot. Because suitable antibodies for detecting CYLD at endogenous levels were not available, a FLAG-HA-tagged CYLD construct was recombinantly expressed for this experiment. This contrasts with the MS-based approach, which relied on endogenous protein levels. Prior to antibody incubation, the membrane was horizontally cut above the 140 kDa marker (expected molecular weight of CYLD: ~110 kDa). The upper part of the blot was probed with an anti-LRRK2 antibody (24D8), while the lower part was probed with anti-FLAG and subsequently re-probed with anti-CYLD antibodies. (**G**) Effect of CYLD co-expression on steady-state LRRK2 levels: LRRK2 WT or Y1699C was co-expressed with CYLD or empty vector control. LRRK2 protein levels were normalized by β-actin. Statistical significance was assessed using unpaired two-tailed *t* tests (*P* values: **A**, **B**: 0.0951; **C**, **D**: 4.5E-8; $N = 6$ biological replicates; error bars = SD) (left panel). Reconstructed Capillary Western signals and confirmation of CYLD expression by western blot. On the capillary western blot, LRRK2 migrates at a lower molecular weight (right panel). Source data are available online for this figure.

Table 1. Ten IDs with the highest Jaccard score underlying identified "Cluster 2".

Accession	Gene name	Protein name	Jaccard score
Q5S007	LRRK2	Leucine-rich repeat serine/threonine-protein kinase 2 (bait)	1.000000
Q9NQC7	**CYLD**	**Ubiquitin carboxyl-terminal hydrolase CYLD**	**0.848485**
Q6P2H3	CEP85	Centrosomal protein of 85 kDa	0.846626
Q96JH7	VCPIP1	Deubiquitinating protein VCPIP1	0.834286
Q96L93	KIF16B	Kinesin-like protein KIF16B	0.832335
P78312	FAM193A	Protein FAM193A	0.817647
Q8NEY1	NAV1	Neuron navigator 1	0.817073
Q7Z2T5	TRMT1L	TRMT1-like protein	0.815951
Q5SZL2	CEP85L	Centrosomal protein of 85 kDa-like	0.810127
O95684	CEP43	Centrosomal protein 43	0.809816
Q96RS0	TGS1	Trimethylguanosine synthase	0.798742

The DUB CYLD (bold) shows the highest co-evolution to LRRK2.

the Core group show a significantly higher RMSD of the LRRK2 chain compared to the WD40 group ($P = 4.05E-3$; Fig. 5F), whose interactors bind LRRK2 in both locked and unlocked conformations (see below). In the Core cluster, we found established LRRK2 interactors, such as DVL1-2, confirming the known interaction mechanism through the ROC-COR domains (Sancho et al, 2009). In the same cluster, we also found novel interactors discovered within the BioID set, such as e.g., CYLD interacting through the Core interface in a similar way. A second cluster (WD40) displayed higher likelihood of interaction with the WD40 domain (Fig. 5A,C), with predicted complexes characterized by a similar interface involving the binding of a short, disordered peptide stretch to a conserved crevice formed by β-propeller loops of the WD40 domain (Fig. 5C). WD40 domain binders might bind to LRRK2 in either locked or unlocked conformation (Fig. 5A,F), as also suggested by a bi-modal distribution of the LRRK2 chain RMSD (Fig. 5F). These interactors also displayed significantly higher co-evolution with respect to "Other" LRRK2 interactors ($P = 5.57E-4$; Fig. 5G). The ARM cluster involves proteins showing binding preferences for a new docking site on the Armadillo domain, centered around residues 500–600 and mediating the interaction with proteins such as AXIN1 (Fig. 5A,D). The larger cluster (Other) contains proteins interacting with weaker likelihood and variable docking sites (Fig. 5A). Among these, we also found proteins engaging with two additional ARM docking sites, including one (around aa 240) which has been recently shown to interact with RAB12 (Dhekne et al, 2023; Li et al, 2024) and mediate a RAB29-independent LRRK2 Kinase activity activation (Purlyte et al, 2018; Zhu et al, 2023), which is predicted to interact with proteins such as KIF16B. A third ARM binding region, encompassing aa 354–444, corresponds to the RAB29 interaction interface found in the recently determined RAB29-bound, tetrameric LRRK2 structure (Zhu et al, 2023), and it is the predicted interface for proteins such as NBR1 and MON2.

Overall, these results further support the hypothesis that interactors de novo identified by proximity labeling may physically interact with LRRK2 domains through specific conformations and contact interfaces. Interactors lacking a strong interaction probability in the distogram might represent proteins interacting with LRRK2 either transiently or indirectly.

Type I but not type II inhibitors lead to conformational changes directing LRRK2 to centriolar satellites

As mentioned above, LRRK2 adopts multiple conformations through which it engages with its interactors. Effector-mediated oligomerization to an asymmetric tetramer has been demonstrated to switch LRRK2 to an active conformation (Zhu et al, 2023). In addition, ATP-competitive kinase inhibitors can stabilize different conformations. While type I inhibitors stabilize the kinase domain in an active-like conformation, type II inhibitors stabilize the inactive conformation of the kinase domain (Deniston et al, 2020; Raig et al, 2025; Zhu et al, 2024). Interestingly, type I but not type II inhibitors lead to a rapid dephosphorylation of LRRK2 phospho-sites in an interdomain space downstream of the hinge-helix, which locks LRRK2 in a compact inactive fold by binding the C-terminal WD40 domain (Kalogeropoulou et al, 2022; Myasnikov et al, 2021). We hypothesized that

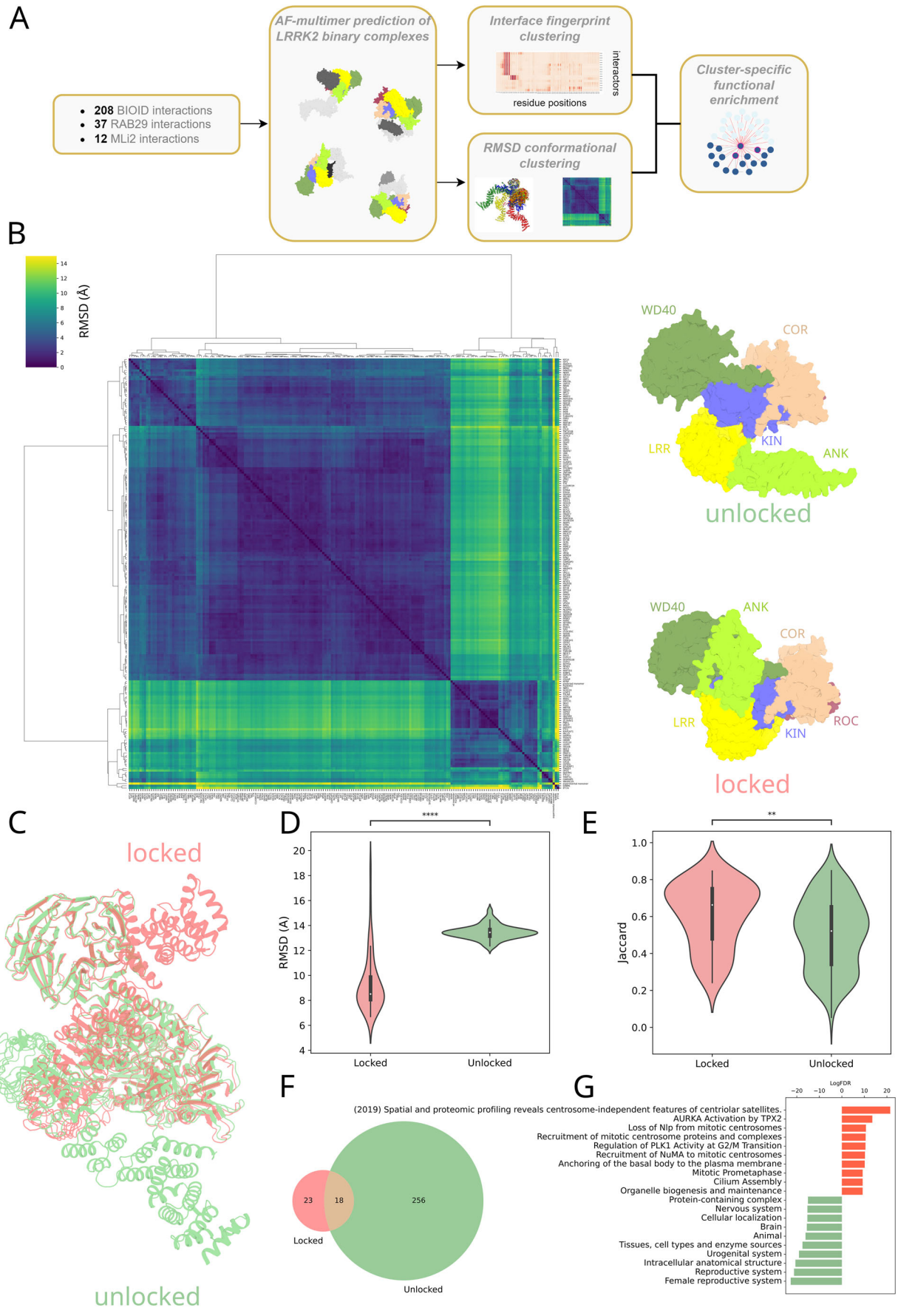
A
AF-multimer prediction of LRRK2 binary complexes
208 BIOID interactions
37 RAB29 interactions
12 MLi2 interactions
Interface fingerprint clustering
interactors
residue positions
RMSD conformational clustering
Cluster-specific functional enrichment
B
RMSD (Å)
WD40
COR
LRR
KIN
ANK
unlocked
WD40
ANK
COR
LRR
KIN
ROC
locked
C
locked
unlocked
D
****
RMSD (A)
Locked
Unlocked
E
**
Jaccard
Locked
Unlocked
F
23
18
256
Locked
Unlocked
G
LogFDR
(2019) Spatial and proteomic profiling reveals centrosome-independent features of centriolar satellites.
AURKA Activation by TPX2
Loss of Nlp from mitotic centrosomes
Recruitment of mitotic centrosome proteins and complexes
Regulation of PLK1 Activity at G2/M Transition
Recruitment of NuMA to mitotic centrosomes
Anchoring of the basal body to the plasma membrane
Mitotic Prometaphase
Cilium Assembly
Organelle biogenesis and maintenance
Protein-containing complex
Nervous system
Cellular localization
Brain
Animal
Tissues, cell types and enzyme sources
Urogenital system
Intracellular anatomical structure
Reproductive system
Female reproductive system

Figure 4. Structural modeling and conformational clustering of the LRRK2 interactome.

3D complexes prediction and analysis of LRRK2 interactome (**A**) Workflow of the structural bioinformatics analysis of LRRK2 interactome. (**B**) On the left, the heatmap showing the hierarchical clustering based on pairwise RMSD calculation of LRRK2's chain in the different complexes. On the right two representative conformations of LRRK2 in the "locked" and "unlocked" conformation to mark the two main clusters. (**C**) Cartoon representation of "locked" (tomato) and "unlocked" (light green) superimposed LRRK2 conformations. (**D**) Violin plot of the distribution of RMSD calculated with respect to the reference LRRK2 experimental structure (PDB 7LHW) for the locked and unlocked clusters ($P = 3.8E-20$; comparison between 48 locked and 148 unlocked independent samples). Color scheme as in (**C**). (**E**) Distribution of the Jaccard score for the locked and unlocked clusters ($P = 0.0013$; comparison between 48 locked and 148 unlocked independent samples). Color scheme as in (**C**). *P* values for violin plots in (**D**, **E**) have been computed with a two-sided Mann–Whitney test (*$P < 0.05$, **$P < 0.01$, ***$P < 0.001$, ****$P < 0.0001$). Violin plots show the median as the white central dot and first and third quartiles as bounds of the thicker black line (box); the whiskers extend to the last data point within 1.5 times the interquartile range (IQR) from the box's boundaries. (**F**) Venn diagram of the enriched terms in the locked and unlocked clusters. Color scheme as in (**C**). (**G**) Top ten exclusively enriched (FDR < 0.01) terms in the locked and unlocked clusters.

specific inhibitors could distinguish the proximity proteome of LRRK2 in its active versus inactive conformation. To test this, we compared the LRRK2 proximity proteome in HEK293 cells stably expressing miniTurbo-tagged LRRK2 following treatment with the type I kinase inhibitor MLi-2, the type II inhibitor GZD-824 (previously shown to inhibit LRRK2 in cells (Kalogeropulou et al, 2022; Tasegian et al, 2021)), or a DMSO control. Western blot analysis of LRRK2 pS935 and pT73-Rab10 confirmed effective inhibition under these conditions (Appendix Fig. S6A). Quantitative label-free analysis combined with an FDR-controlled *t* test revealed that only MLi-2 treatment led to the enrichment of a distinct set of proteins associated with cilia assembly and centriolar satellites in the LRRK2 proximity proteome (Fig. 6A–E; Appendix Fig. S6B), a pattern not observed with GZD-824. Intriguingly, interactors determined in the presence of the MLi-2 inhibitor are characterized by a significantly higher co-evolution (Fig. 6F) compared to other BioID interactors. The complete list of significantly enriched proteins (MLi-2 vs. DMSO) is shown in Table 2. Additional information is provided in Dataset EV1.

To functionally validate the interaction between LRRK2 and centriolar satellites, we first confirmed that LRRK2 associates with key components of these membrane-less organelles, including the central scaffold protein PCM1 and the centrosome maturation factor SSX2IP (Barenz et al, 2013). Both proteins were enriched in LRRK2 proximity proteomes following biotin treatment, with their interaction further enhanced by the LRRK2 inhibitor MLi-2. To further substantiate LRRK2's association with centriolar satellites, we employed RNA interference to deplete PCM1, a strategy known to disrupt satellite integrity (Dammermann and Merdes, 2002). As expected, PCM1 depletion led to its absence from the LRRK2 proximity proteome and also abolished the association between LRRK2 and SSX2IP. Remarkably, SSX2IP was entirely absent from LRRK2 proteomes regardless of MLi-2 treatment, indicating that LRRK2's interaction with SSX2IP is dependent on intact centriolar satellites. Finally, we asked whether the MLi-2–induced dephosphorylation of serine 935—located near the LRRK2 hinge helix—is affected by satellite disruption. However, PCM1 knockdown did not influence serine 935 dephosphorylation, suggesting that this post-translational modification occurs independently of centriolar satellite integrity (Fig. 6D; Appendix Fig. S6C).

RAB29 co-expression directs LRRK2 to well-established lysosomal protein networks

It has been previously shown that LRRK2 interacts with the RAB29/RAB32/RAB38 family of small G-proteins and subsequently locates to post-Golgi endomembranes (Beilina et al, 2014; McGrath et al, 2021; Vides et al, 2022; Waschbusch et al, 2014). Furthermore, RAB29 not only recruits LRRK2 to lysosomal membranes but also induces its tetramerization (Zhu et al, 2023). For this reason, we performed the BioID experiment following RAB29 co-expression to determine PPI networks associated with the activated oligomeric state of LRRK2. In addition to mT-LRRK2, either RAB29 or an empty vector was co-expressed. The resulting differential proximity proteome showed differentially enriched proteins only for the condition where RAB29 was co-expressed, demonstrating that a small portion of LRRK2 was recruited by RAB29 with lesser impact on the total proximity proteome (Fig. 6G). While we did not observe any significant difference in terms of co-evolution of the RAB29 differential proteome with respect to the BioID one (Fig. 6F), we found significant enrichment in proteins involved in vesicular transport, including the post-Golgi/ lysosomal compartment, as revealed by an LFQ analysis combined with an FDR-controlled *T* test (Fig. 6H,I). In particular, known LRRK2 effectors, namely RAB8A (Steger et al, 2017) and SPAG9 (Boecker and Holzbaur, 2021; Bonet-Ponce et al, 2020; Kluss et al, 2022a) were among the enriched proteins (Fig. 6G,H). Also, VAMP7, which is part of a SNARE complex mediating autophagosome-lysosome fusion (Jian et al, 2024), was among the significantly enriched proteins (Fig. 6G,H). VAMP7-LRRK2 physical interaction has recently been described (Filippini et al, 2023). The complete list of significantly enriched proteins is shown in Table 3. Additional information is provided in Dataset EV1.

MLi-2 and RAB29 differently modulate the shape of the LRRK2 interactome

We constructed 3D models of binary complexes between LRRK2 and its partners from the MLi-2– and RAB29-dependent interactomes and examined both the complex interfaces and the conformational states of LRRK2 (Vides et al, 2022).

Interface-based clustering suggests that MLi-2–dependent interactors engage with LRRK2 through specific domain regions, particularly the ones involving terminal domains (Fig. EV1A), while they are predicted to engage little with the catalytic domains, particularly the kinase, which is consistent with the MLi-2 inhibitor function. In the RAB29-dependent LRRK2 interactome, we see instead a more variable pattern of engaged interfaces. In particular, predictions for this interactome revealed a cluster of proteins interacting with LRRK2 through the ROC-COR-KIN domains, including the RAB8A substrate (Fig. EV1B), suggesting that in the context of RAB29 overexpression, several partners might bind in a substrate-like manner. Notably, this interaction modality is absent in the predicted binary complexes of the MLi-2–bound interactome, confirming that the inhibitor prevents LRRK2 from

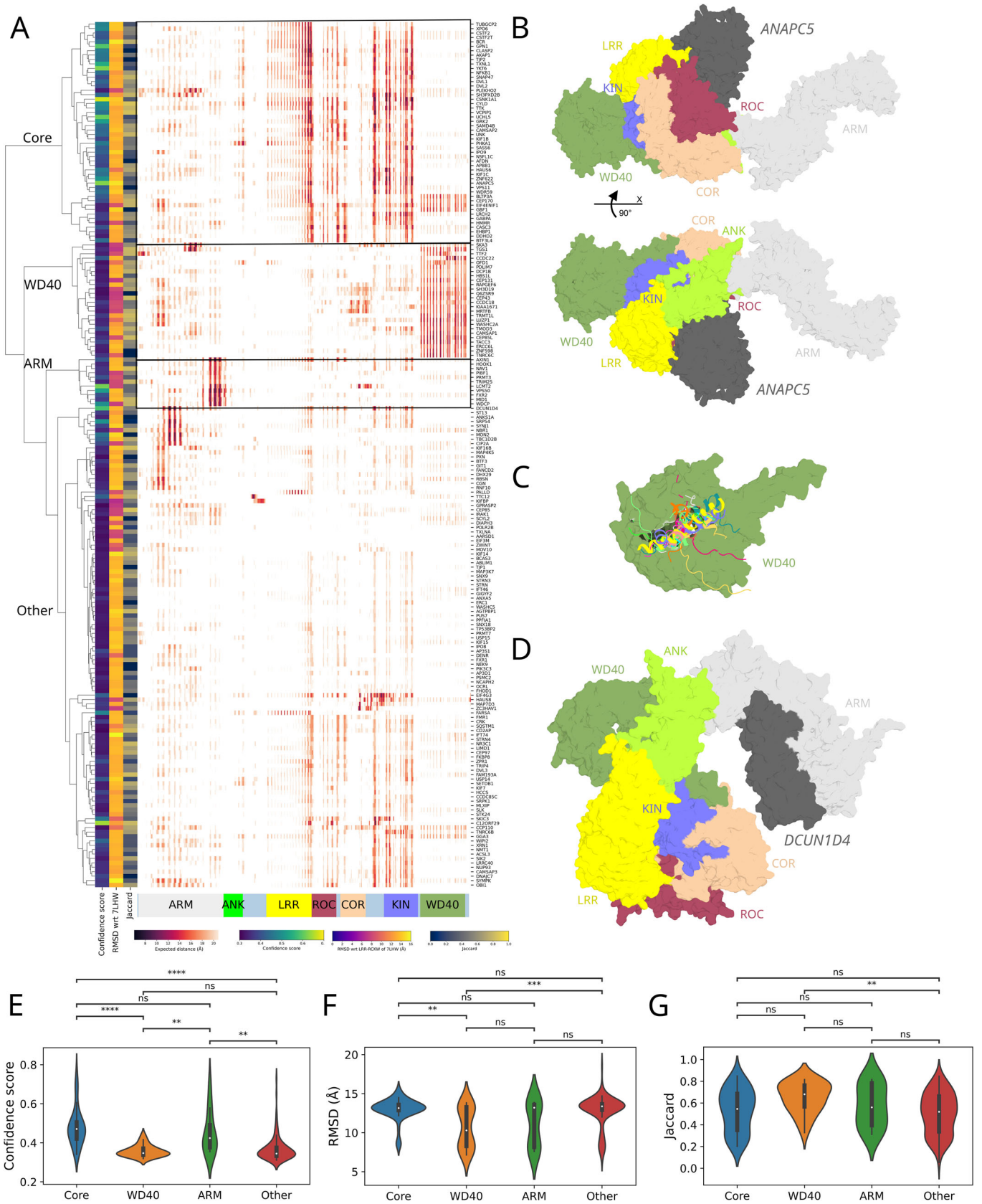
A
Core
WD40
ARM
Other
Confidence score
RMSD wrt 7LHW
Jaccard
ARM
ANK
LRR
ROC
COR
KIN
WD40
Expected distance (Å)
Confidence score
RMSD wrt LRR-RCKW of 7LHW (Å)
Jaccard
B
ANAPC5
LRR
KIN
ROC
ARM
WD40
COR
90°
X
COR
ANK
KIN
ROC
WD40
ARM
LRR
ANAPC5
C
WD40
D
ANK
WD40
ARM
KIN
DCUN1D4
COR
LRR
ROC
E
Confidence score
Core
WD40
ARM
Other
F
RMSD (Å)
Core
WD40
ARM
Other
G
Jaccard
Core
WD40
ARM
Other

Figure 5. Interface analysis of predicted LRRK2 binary complexes.

Interface analysis of LRRK2's 3D interactome (**A**) Interface fingerprint of the LRRK2 complexes via distogram calculation. Cells contain the minimum expected distance obtained from the distograms of any residue of each interactor (row) to every residue in LRRK2 (column). Rows are color annotated based on confidence score, Jaccard and RMSD from reference LRRK2 structure (PDB: 7LHW). (**B**) Representative structure of the Core cluster (i.e., LRRK2-ANAPC5 complex). (**C**) Representative structures of the WD40 cluster. (**D**) Representative structures of the ARM binding mode cluster (i.e., LRRK2- DCUN1D4 complex). Distribution among different interface cluster of the (**E**) confidence score, (**F**) RMSD and (**G**) Jaccard score descriptors. (**C–E**) show the comparison between 196 independent samples divided into 4 clusters with the following number of elements: 50 Core, 26 WD40, 11 ARM and 109 Other. *P* values have been computed with a two-sided Mann–Whitney test with Bonferroni correction (*$P < 0.05$, **$P < 0.01$, ***$P < 0.001$, ****$P < 0.0001$). Violin plots show the median as the white central dot and first and third quartiles as bounds of the thicker black line (box); the whiskers extend to the last data point within 1.5 times the interquartile range (IQR) from the box boundaries. (**C**) *P* values: Core-WD40: 1.1E-8; Core-ARM: 1.0; Core-Other: 4.9E-14; WD40-ARM: 0.0035; WD40-Other: 1.0; ARM-Other: 0.0030. (**D**) *P* values: Core-WD40: 0.0040; Core-ARM: 1.0; Core-Other: 1.0; WD40-ARM: 1.0; WD40-Other: 5.6E-4; ARM-Other: 1.0. (**E**) *P* values: Core-WD40: 0.099; Core-ARM: 1.0; Core-Other: 1.0; WD40-ARM: 1.0; WD40-Other: 0.0026; ARM-Other: 1.0.

binding substrate-like partners. Moreover, we further validated the capability of the distogram-based interface-fingerprint to discriminate functionally relevant LRRK2 interactors. We predicted 3D complexes between LRRK2 and known interacting Rabs and found that Rab substrates clustered separately from other interacting Rabs with distinct functions, such as RAB29 and RAB32 (Fig. EV1B).

From a conformational perspective, we pooled the RAB29- and MLi-2–dependent interactomes and clustered LRRK2 structures based on RMSD, which likewise revealed distinct locked and unlocked clusters (Fig. 7A). Interestingly, Rab8a acting downstream of LRRK2 and RAB29 acting upstream of LRRK2 engage with LRRK2 in two different conformations: While RAB8A engages with the unlocked state (Fig. 7B), structural modeling suggests that RAB29 engages with the locked state (Fig. 7C). Interactors from the RAB29-dependent interactome are predicted to bind LRRK2 in both conformations, with a particular enrichment in the unlocked state. Conversely, MLi-2–dependent interactors were significantly enriched in the locked LRRK2 conformation (Fisher's exact test, $P = 0.023$), further suggesting that the inhibitor-bound state favors engagement with partners that, unlike substrates, do not require interaction with the kinase domain (Fig. 7A). Also for these interactors, the locked conformation has a significantly lower RMSD ($P = 3.85E\text{-}6$; Fig. 7D) and a tendency towards higher co-evolution (Fig. 7E). Notably, enrichment analysis of interaction partners grouped by conformational cluster revealed even stronger cluster-specific associations, with only a single process shared between partners in the locked and unlocked conformations (Fig. 7F,G; Dataset EV2E).

Discussion

The systematic analysis of the interactomes of disease-associated proteins is a powerful tool to dissect molecular networks and to identify pathways relevant for the molecular pathophysiology, for example, demonstrated by the comprehensive interactomic network underlying the assembly and homeostasis of primary cilia (Boldt et al, 2016). Given its complex domain structure and tight regulation, LRRK2 is most likely representing a scaffold protein orchestrating distinct signaling complexes, which makes the analysis of its PPI networks an attractive approach to dissect context-specific signaling pathways (Gloeckner and Porras, 2020). While a wealth of data is available for affinity-based identification of protein–protein interactions, which are biased toward stable complexes, there is an unmet need for the dissection of less stable and transient PPIs. The rapid development of biotin-based proximity labeling technologies has made it possible to explore previously inaccessible regions of the interactome (Qin et al, 2021). Consequently, APEX and BioID have emerged as widely used techniques for dissecting protein–protein interaction (PPI) networks (Li et al, 2017). For LRRK2, the first APEX2 dataset only recently became available (Bonet-Ponce et al, 2020). In the present study, we systematically investigated the proximity interactome of LRRK2 using three different BioID tags—BioID1, BioID2, and miniTurbo. The resulting data showed the expected overlap with previously reported interactors, while also uncovering numerous novel candidates. However, several anticipated interactors, including Rab proteins, were not detected in the initial BioID experiments. Nevertheless, RAB8A was identified together with RAB29 upon co-expression of RAB29, which may reflect conformational constraints that reduce accessibility for BioID-mediated biotinylation. Consistent with these observations, a recent comparison of BioID and co-immunoprecipitation in the context of the nuclear pore complex demonstrated that the two approaches provide functionally relevant yet complementary interaction profiles (Moreira et al, 2023).

To identify direct LRRK2 interactors with high confidence from the proximity proteomes, we applied a newly developed bioinformatic pipeline relying on co-evolution, co-expression, and protein domain architecture to predict interaction type (preprint: Miglionico et al, 2024). This pipeline allowed the identification of a group of proteins within the proximity proteome showing a high degree of co-evolution with LRRK2, which is highly enriched in proteins associated with the centrosome. This is particularly interesting as pathogenic LRRK2 has previously been shown to lead to a centrosome cohesion defect as well as to a shortening of primary cilia (Dhekne et al, 2018; Khan et al, 2024; Lara Ordonez et al, 2022). Furthermore, defects in primary cilia emerge as a new pathophysiological scheme connecting different genes involved in Mendelian forms of Parkinson's disease (Mohd Rafiq et al, 2024; Schmidt et al, 2022). Strikingly, within the cluster of proteins showing the highest co-evolution with LRRK2 (Cluster 2), the top-ranked interactor was the deubiquitinase CYLD, a key effector in primary cilia biology. Preliminary data further indicate that CYLD co-expression increases the levels of the pathogenic LRRK2 Y1699C variant, which exhibits lower steady-state protein levels than wild-type LRRK2. In fact, this DUB has been shown to control apical docking of basal bodies in ciliated epithelial cells (Eguether et al, 2014). It also regulates centrosomal satellites proteostasis by counteracting the E3 ubiquitin ligase MIB1 (Douanne et al, 2019). CYLD has also been shown to deubiquitinate Cep70 and to inactivate HDAC6 thereby mediating ciliogenesis (Yang et al, 2014). Interestingly, a missense mutation has recently been shown to be a causative gene for FTD-ALS (Dobson-Stone et al, 2020).

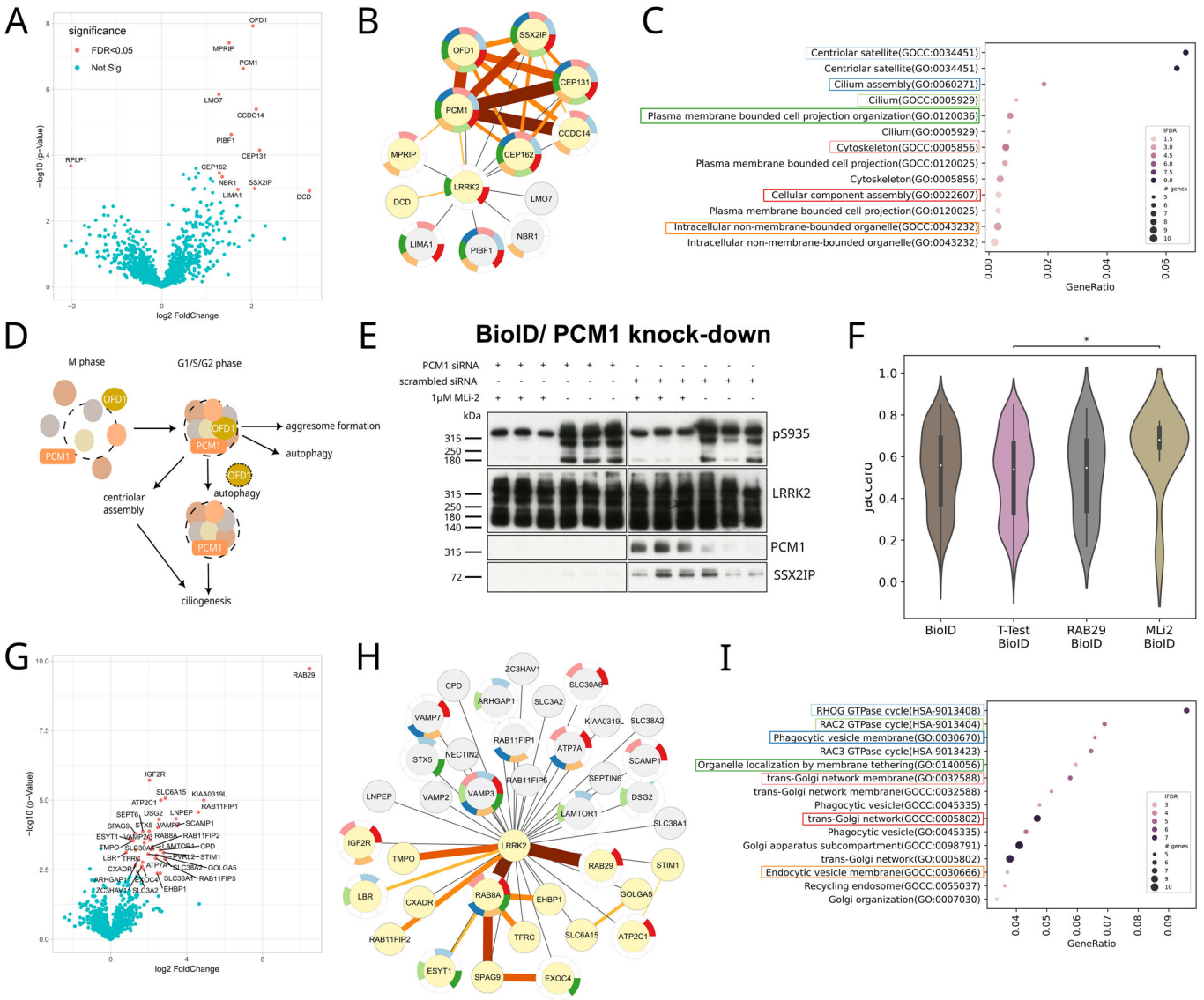

Figure 6. Different effects of type I and type II inhibitors and RAB29 on the LRRK2 proximity proteome.

(**A**) Volcano plot MLi-2 vs DMSO (moderated permutation-based *T* test, FDR = 0.05; S0 = 0.1, *N* = 7). (**B**) Stringified network of the MLi-2 interactome from (**A**) mapped to IntAct known interactions. Edges' color and thickness for mapped interactions are proportional to IntAct MI score, else they are colored in gray with constant thickness. Node rims are colored according to enriched processes; (**C**) Dot plot showing top 15 significantly enriched (FDR < 0.01) categories from the LRRK2-MLi-2 interactome. Values on the *x* axis display the ratio of genes of the term participating to the network over the total number of genes in that category. The size of the dot is proportional to the number of genes of that category in the network, while the node color is the darker the more significant is the category enrichment. Only categories with at least 5 genes have been displayed. Representative, enriched categories have been colored with the same color scheme as in (**C**). (**D**) Scheme highlighting the function of centriolar satellites and the core protein PCM1 in ciliation (Hori and Toda, 2017, modified) (**E**) BioID analysis following PCM1 knockdown and MLi-2 treatment. Shown eluates are obtained after streptavidin-based enrichment of biotinylated proteins. (**F**) Violin plot reporting the Jaccard Score distribution in different datasets. *P* values have been computed with a two-sided Mann–Whitney test with Bonferroni correction (*$P < 0.05$; $P = 0.0499$ for *T* test BioID vs MLi-2 BioID; comparison between 188 BioID, 431 *T* test BioID, 36 RAB29 BioID and 9 MLi-2 BioID independent samples; only *P* values < 0.05 are shown). Violin plots show the median as the white central dot and first and third quartiles as bounds of the thicker black line (box); the whiskers extend to the last data point within 1.5 times the interquartile range (IQR) from the box boundaries. (**G**) Volcano plot (+/−RAB29): mT-LRRK2 proximity proteome following RAB29 co-expression (moderated FDR-based *T* test, $P = 0.05$; S0 = 0.1, *N* = 9). RAB29 redirects LRRK2 to lysosomal PPI networks. (**H**) Stringified network of the RAB29 overexpression interactome from (**G**) mapped to IntAct known interactions. Edges' color and thickness for mapped interactions are proportional to IntAct MI score, else they are colored in gray with constant thickness. Node rims are colored according to enriched processes. (**I**) Dot plot showing top 15 significantly enriched (FDR < 0.01) categories from the LRRK2-RAB29 overexpression interactome. Values on the *x* axis display the ratio of genes of the term participating to the network over the total number of genes in that category. The size of the dot is proportional to the number of genes of that category in the network; the darker the node color, the more significant the category enrichment. Only categories with at least five genes have been displayed. Representative, enriched categories have been colored with the same color scheme as in (**H**).

Table 2. Enriched proteins in the LRRK2 proximity proteome upon MLi-2 treatment (FDR-controlled *T* test).

Accession	Protein name	Gene name	*P* value (-log10)	Log2 *T* test difference
P81605	Dermcidin	DCD	2.91844	3.3
Q9UPN4	Centrosomal protein of 131 kDa	CEP131	4.15494	2.2
Q49A88	Coiled-coil domain-containing protein 14	CCDC14	5.39373	2.1
Q9Y2D8	Afadin- and alpha-actinin-binding protein	SSX2IP	2.98866	2.1
O75665	Oral-facial-digital syndrome 1 protein	OFD1	7.92350	2.0
Q15154	Pericentriolar material 1 protein	PCM1	6.62987	1.8
Q9UHB6	LIM domain and actin-binding protein 1	LIMA1	2.96451	1.7
Q8WXW3	Progesterone-induced-blocking factor 1	PIBF1	4.62801	1.5
Q6WCQ1	Myosin phosphatase Rho-interacting protein	MPRIP	7.40967	1.5
Q14596	Next to BRCA1 gene 1 protein	NBR1	3.34347	1.3
Q5TB80	Centrosomal protein of 162 kDa	CEP162	3.46643	1.3
Q8WWI1	LIM domain only protein 7	LMO7	5.84664	1.3

Most importantly, as the deubiquitinase CYLD is part of the PINK1/Parkin pathway to regulate cellular levels of PARIS (ZNF746), it is a critical regulator of mitochondrial biogenesis thereby acting as a negative regulator of dopamine neuron survival in Parkinson's disease. In fact, CYLD inhibition has been shown to ameliorate mitochondrial pathologies in cellular PD models, which makes CYLD a promising target for therapeutic intervention for PD and other neurodegenerative diseases (Pirooznia et al, 2022). The E3 ligase Parkin preserves mitochondrial homeostasis via the PARIS/PGC-1a axis (Stevens et al, 2015; Zheng et al, 2017). Notably, the PD risk variant LRRK2 G2385R has recently been shown to alter mitochondrial biogenesis via the PGC-1a pathway, leading to reduced PGC-1a levels, similar to a Parkin knock-out in DA neurons (Kumar et al, 2020; Xue et al, 2023). Parkin-deficient DA neurons show increased PARIS and decreased PGC-1a levels (Kumar et al, 2020). In conclusion, this indicates that LRRK2/CYLD signaling, on one hand, and Parkin signaling, on the other, might converge on PARIS.

The second most co-evolved interactor found in Cluster 2 was the cilia-associated protein CEP85, which plays a role in centrosome disjunction (Chen et al, 2019). This is of particular interest as pathogenic LRRK2 variants lead to a centrosomal cohesion phenotype in patient-derived cells (Lara Ordonez et al, 2019). Notably, the cohesion phenotype is also seen in EBV-transformed lymphoblastoid cell lines from iPD patients, which can be reverted by LRRK2 kinase inhibition (Naaldijk et al, 2024). Importantly, Cluster 2 also contains the autophagy cargo protein p62/sequestosome-1. This protein has previously been identified as LRRK2 interactor and substrate (Kalogeropulou et al, 2018; Park et al, 2016). SQSTM1 is also linked to PD pathophysiology via the Pink1/Parkin pathway (Shin et al, 2020). In addition, Cluster 2 points towards other pathways that have been previously linked to PD pathology. In particular, SNAP47 is part of the STX17-SNAP47-VAMP7/8 pathway, which has been shown to be involved in selective autophagy – a process not only essential for the homeostasis of primary cilia but also for mitophagy (Jian et al, 2024). Phospho-ubiquitin chains generated by PINK1/Parkin activity can recruit autophagy adapters, including the ubiquitin adapter SQSTM1/p62, linking the PINK1/Parkin-dependent pathway to mitophagy (Geisler et al, 2010). All three proteins participate in the recruitment of the autophagy machinery to aged or dysfunctional mitochondria, which are eventually enclosed inside an autophagosome and subjected to the lysosome for degradation (Wilhelm et al, 2022).

Interestingly, the kinesin motor protein KIF16B, a PX domain-containing protein, was also among the top hits. KIF16B is involved in vesicle trafficking and receptor recycling, binds phosphatidylinositol 3-phosphate [PI(3)P] via its PX domain, and promotes cargo transport from early endosomes to the plasma membrane (Li et al, 2020). Interestingly, it has been found to be associated with lipid droplets (Bersuker et al, 2018). In turn, increased RAB8a phosphorylation by pathogenic LRRK2 variants has been shown to promote lipid storage (Yu et al, 2018), indicating that the functional interaction of LRRK2 and KIF16B might contribute to alterations in the neuronal lipid homeostasis associated with PD pathology (Hallett et al, 2019).

Furthermore, conformational changes induced by MLi-2 binding—leading to rapid and nearly complete dephosphorylation of LRRK2 within a disordered domain downstream of the hinge helix—position LRRK2 in proximity to a molecular network centered around PCM1, OFD1, and CEP131, strongly supporting a link between LRRK2 and centriolar satellites. Strikingly, the proteins interacting with LRRK2 in the presence of MLi-2 displayed the highest degree of co-evolution, suggesting that the connection between LRRK2 and centriolar satellites is highly conserved. The conformational changes induced by the binding of type I inhibitors might result in a phase transition of LRRK2 into centriolar satellites preventing 14-3-3 binding and thereby shifting the equilibrium towards the dephosphorylated protein. A similar mechanism has been shown for CEP131, which is extracted from centriolar satellites by phosphorylation and subsequent binding of 14-3-3 (Tollenaere et al, 2015). Centriolar satellites not only play an essential role in the biogenesis of primary cilia (Hall et al, 2023) but also play a role in the degradation of proteins by driving the assembly of aggresomes (Prosser et al, 2022). In fact, LRRK2 has also been shown to interfere with aggresome formation preceding autophagic clearance (Bang et al, 2016). Nevertheless, one caveat might be seen in the fact that LRRK2 inhibition with type I inhibitors induces its destabilization and degradation (Lobbestael et al, 2016).

Table 3. Enriched proteins in the RAB29-dependent LRRK2 proximity proteome (FDR-controlled *T* test).

Accession	Protein name	Gene name	*P* value (−log10)	Log2 *T* test difference
O14966	Ras-related protein Rab-7L1	RAB29	9.72545	10.5
Q8IZA0	Dyslexia-associated protein KIAA0319-like protein	KIAA0319L	5.00209	4.9
Q6WKZ4	Rab11 family-interacting protein 1	RAB11FIP1	4.56815	4.6
O15126	Secretory carrier-associated membrane protein 1	SCAMP1	4.09385	3.5
Q9UIQ6	Leucyl-cystinyl aminopeptidase; Leucyl-cystinyl aminopeptidase, pregnancy serum form	LNPEP	4.33552	3.4
Q9H2J7	Sodium-dependent neutral amino acid transporter B(0)AT2	SLC6A15	5.06972	2.9
Q96QD8	Sodium-coupled neutral amino acid transporter 2	SLC38A2	2.89271	2.9
Q13586	Stromal interaction molecule 1	STIM1	3.12115	2.8
P98194	Calcium-transporting ATPase type 2 C member 1	ATP2C1	5.00347	2.6
Q9H2H9	Sodium-coupled neutral amino acid transporter 1	SLC38A1	2.37723	2.6
O75976	Carboxypeptidase D	CPD	3.20952	2.6
Q14126	Desmoglein-2	DSG2	4.31421	2.5
P51809	Vesicle-associated membrane protein 7	VAMP7	4.02209	2.5
Q8NDI1	EH domain-binding protein 1	EHBP1	2.37346	2.5
Q8TBA6	Golgin subfamily A member 5	GOLGA5	3.0259	2.4
Q9BXF6	Rab11 family-interacting protein 5	RAB11FIP5	2.9101	2.4
Q7L804	Rab11 family-interacting protein 2	RAB11FIP2	3.33154	2.2
Q6IAA8	Ragulator complex protein LAMTOR1	LAMTOR1	3.23604	2.1
P61006	Ras-related protein Rab-8A	RAB8A	3.56486	2.1
P11717	Cation-independent mannose-6-phosphate receptor	IGF2R	5.71543	2.0
Q13190	Syntaxin-5	STX5	3.88884	2.0
Q15836;P63027	Vesicle-associated membrane protein 3; Vesicle-associated membrane protein 2	VAMP3;VAMP2	3.67019	2.0
Q92692	Nectin-2	PVRL2	3.06334	2.0
Q6NXT4	Zinc transporter 6	SLC30A6	3.47208	1.8
Q96A65	Exocyst complex component 4	EXOC4	2.51947	1.7
Q14141	Septin-6	Sept6	3.87782	1.7
Q04656	Copper-transporting ATPase 1	ATP7A	2.77415	1.7
Q7Z2W4	Zinc finger CCCH-type antiviral protein 1	ZC3HAV1	2.62567	1.6
P78310	Coxsackievirus and adenovirus receptor	CXADR	2.87956	1.4
P08195	4F2 cell-surface antigen heavy chain	SLC3A2	2.43497	1.4
P02786	Transferrin receptor protein 1; Transferrin receptor protein 1, serum form	TFRC	3.21618	1.3
Q07960	Rho GTPase-activating protein 1	ARHGAP1	2.65929	1.3
O60271	C-Jun-amino-terminal kinase-interacting protein 4	SPAG9	3.80826	1.3
P42167	Lamina-associated polypeptide 2, isoforms beta/gamma; Thymopoietin; Thymopentin	TMPO	3.54449	1.2
Q9BSJ8	Extended synaptotagmin-1	ESYT1	3.59064	1.0
Q14739	Lamin-B receptor	LBR	3.12029	0.8

Structural prediction of LRRK2 binary complexes with AF revealed distinct interfaces within each determined interactome. While several interactors preferentially engage with the catalytic core of the protein, including the ROC and KIN domains, others are more likely to interact with terminal domains (e.g., ARM or WD40). We predicted the interaction on the kinase domain for several interactors of the BioID interactome, as well as the one obtained in the presence of RAB29 overexpression, including the known substrate RAB8A. The engagement in a substrate-like fashion with the catalytic core entails the opening of the LRRK2 structure, with the detachment of the LRR and rearrangement of the entire N-term domains. We previously showed that this conformation, which we similarly predicted for the LRRK2:RAB10 complex, is compatible with distance restraints obtained by mass

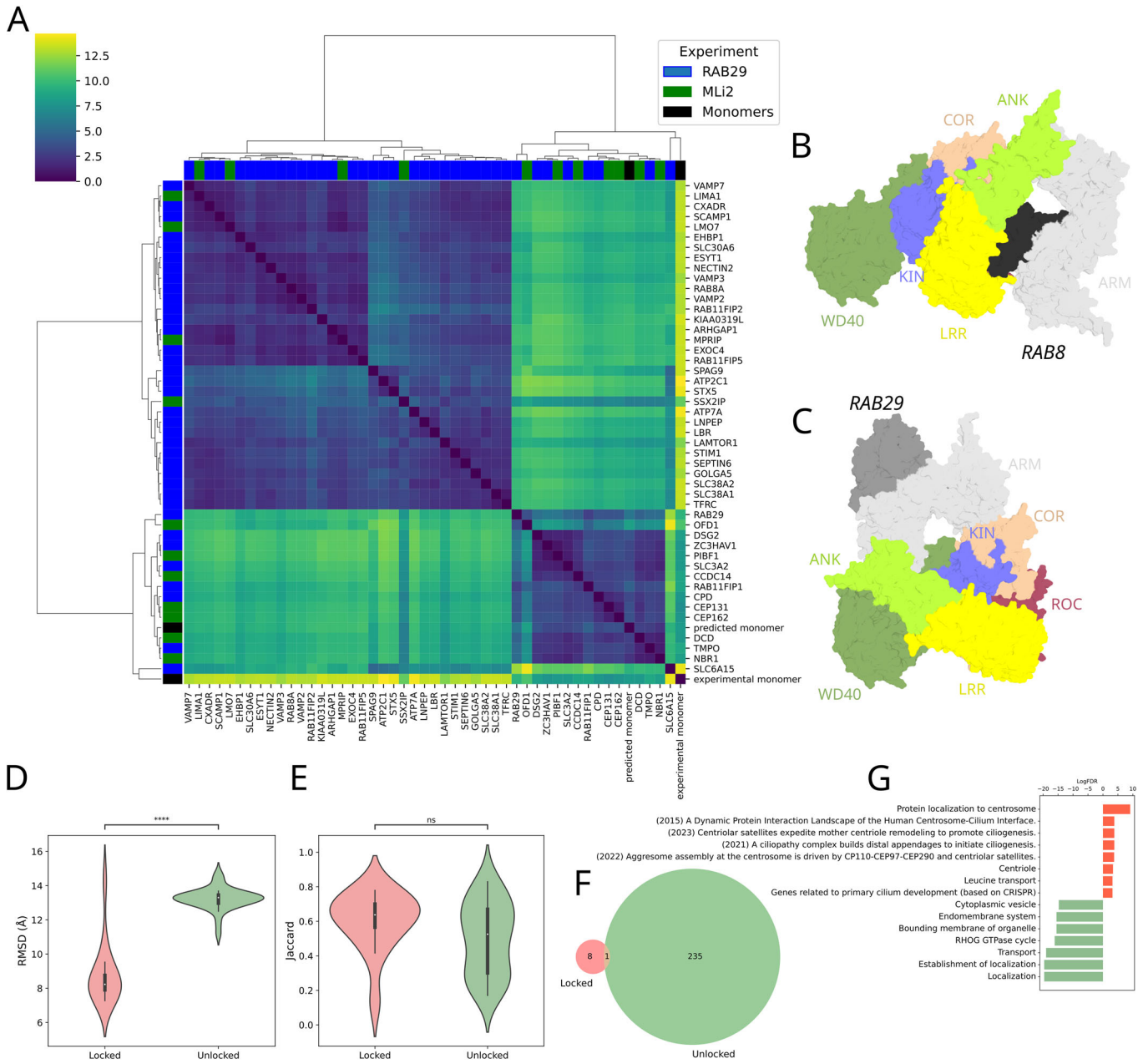

Figure 7. AF-structural modeling of MLi-2 and RAB29 interactomes.

(**A**) Hierarchical clustering of pairwise RMSD of LRRK2 chain in the different complexes. (**B**) LRRK2-RAB8A predicted complex. (**C**) LRRK2-RAB29 predicted complex. (**D**) Violin plot of the distribution of RMSD calculated with respect to the reference LRRK2 experimental structure (PDB 7LHW) for the locked and unlocked clusters. Color scheme as in 4 C ($P = 3.8E\text{-}6$; comparison between 14 locked and 32 unlocked independent samples). (**E**) Distribution of the Jaccard score for the locked and unlocked clusters ($P = 0.14$; comparison between 14 locked and 32 unlocked independent samples). Color scheme as in Fig. 4C. *P* values in violin plots in (**D**, **E**) have been computed with a two-sided Mann–Whitney test (*$P < 0.05$, **$P < 0.01$, ***$P < 0.001$, ****$P < 0.0001$). Violin plots show the median as the white central dot and first and third quartiles as bounds of the thicker black line (box); the whiskers extend to the last data point within 1.5 times the interquartile range (IQR) from the box's boundaries. (**F**) Venn diagram of the enriched terms in the locked and unlocked clusters. Color scheme as in Fig. 4C. (**G**) Top exclusively enriched (FDR < 0.01) terms in the locked and unlocked clusters. Color scheme as in Fig. 4C.

spectrometric mapping of chemical crosslinking sites via XL-MS (preprint: Guaitoli et al, 2023). Moreover, when superimposed onto the active-like conformation of the most recent LRRK2 tetrameric structure, these predicted complexes fit well within the oligomer, without steric clashes between the modeled LRRK2 chain and the rest of the tetramer, further supporting their structural plausibility (preprint: Guaitoli et al, 2023). We speculate that partners engaging in this manner may represent putative substrates or function as regulators of kinase domain activity. Strikingly, such interaction interfaces were rarely observed among interactors enriched in the presence of the MLi-2 inhibitor, which preferentially binds the locked conformation of LRRK2.

It should be noted that the HEK293T system, while enabling large-scale experimental throughput, may exhibit a cell-type–specific bias, including an overrepresentation of microtubule-binding proteins compared with other cell types. Another limitation is the low endogenous expression of LRRK2 in HEK293T cells. As a result, the study relies on the overexpression of LRRK2 BioID fusion proteins, which may introduce artifacts not present under physiological conditions.

In conclusion, combining proximity proteomics with co-evolutionary and structural information helped identify distinct molecular networks linking LRRK2 to centrosomal biology and primary cilia. The data may foster future functional analysis to further dissect these pathways to get a detailed picture of the molecular pathophysiology underlying the cilia phenotypes caused by genetic variants in different genes underlying familial forms of Parkinson's disease.

Methods

Reagent and tools table

Reagent or resource	Reference or source	Identifier or catalog number
Experimental models		
HEK293	DMSZ	ACC 305
HEK293T	DMSZ	ACC 365
Recombinant DNA		
pcDNA3.0	Invitrogen	N/A
pDONR201 LRRK2	Gloeckner et al, 2010	N/A
pDEST-BioID	This study	N/A
pDEST-BioID2	This study	N/A
pDEST-mT (miniTurbo)	This study	N/A
LRRK2-BioID(1)	This study	N/A
LRRK2-BioID2	This study	N/A
LRRK2-mT (miniTurbo)	This study	N/A
SF-TAP LRRK2-WT	Gloeckner et al, 2010	N/A
SF-TAP LRRK2-Y1699C	This study	N/A
HA-RAB29	This study	N/A
FLAG/HA-CYLD	Addgene	22544
HA-Ubiquitin WT	Treier et al, 1994	N/A
pRK5-HA-Ubiquitin-K63	Addgene	17606
Antibodies		
Ani-LRRK2 (24D8)	Carrion et al, 2017	N/A
Anti-CYLD	Proteintech	66858-1-Ig
Anti-HA (3F10)	Roche	H3663
Anti-FLAG	Sigma-Aldrich	F1804-200UG
Anti-pS935 LRRK2	Abcam	ab133450
Anti-Rab10 pT73	Abcam	ab230261
Anti-Rab10	Abcam	ab181367
Anti-PCM1	Proteintech	19856-1-AP
Anti-SSX2IP	Thermo Fisher Scientific	PA5-31495
Streptavidin-HRP	Thermo Fisher Scientific	10598893
Goat anti-Rat HRP	Jackson Immuno-Research	112-036-062
Goat anti-Mouse HRP	Jackson Immuno-Research	115-036-062
Goat anti-Rabbit HRP	Jackson Immuno-Research	111-036-045
Anti-Rabbit Secondary HRP	Bio-techne	042-206
Anti-Rabbit Secondary IR	Bio-techne	104763
Anti-Mouse Secondary NIR	Bio-techne	104702
Anti-beta-Actin	R&D Systems	MAB8929
Oligonucleotides and sequence-based reagents		
PCM1 (Silencer Silect)	Life Technologies	s10128
Negative Control No. 2	Life Technologies	4390846
Cell culture reagents		
PBS	Thermo Fisher Scientific	14190250
DMEM	Sigma-Aldrich	D6429-500ML
Penicillin-Streptomycin solution	Thermo Fisher Scientific	15140122
FBS	Sigma-Aldrich	F7524-500ML
G418 (Geneticin)	Biochrom	A2912
Chemicals, enzymes, and other reagents		
Biotin	Sigma-Aldrich	B4639
MLi-2	Cayman Chemical Company	19305
GZD-824	Cayman Chemical Company	21508
HPLC water (LC-MS grade)	Merck	1153332500
DMSO	AppliChem	A3672.0050
PEI (Polyethylenimine)	Polysciences	23966
Lipofectamine RNAiMAX	Life Technologies	13778030
PhosSTOP	Roche	4906845001
Complete Protease Inhibitor Cocktail	Roche	11836170001
Nonidet P40 Substitute	Sigma-Aldrich	11754599001
MagStrep Strep-Tactin Resin	IBA	2-1613-002
StrepTactin Superflow resin	IBA	2-1206-025
Desthiobiotin Elution Buffer	IBA	2-1000-025
Hyperfilm ECL	Cytiva	28-9068-37
Microspin columns	Cytiva	27356501
Trypsin	Sigma-Aldrich	T6567-5X20UG
Trypsin/LysC	Promega	V5073
RapiGest	Waters	186001861
Ammonium bicarbonate	Sigma-Aldrich	A6141

Reagent or resource	Reference or source	Identifier or catalog number
DTT	Merck	1114740025
IAA (iodoacetamide)	Merck	8047440025
PP (Polypropylene)-Inserts	Sigma-Aldrich	24722
StageTips (200 µL, C18)	Thermo Fisher Scientific	SP301
TFA (Trifluoracetic Acid)	Sigma-Aldrich	80457-10X1ML
Jess Capillary Western Kit	ProteinSimple	SM-W003
ECL+	Thermo Fisher Scientific	32132
BCA assay	Thermo Fisher Scientific	23227
Software		
AlphaFold-Multimer	DeepMind	v2.3.2
MaxQuant	Max Planck Institute	v2.0.3.1
Perseus	Max Planck Institute	v1.6.7
Uniprot database	Uniprot.org	Release 2021_04
SAINTExpress	Teo et al, 2014	N/A
Cytoscape	The Cytoscape Consortium	v3.8.2
ProteoRE server	Proteore.org	Galaxy v2021.05.12
Python (SciPy, Matplotlib)	Python.org	v3.10
PDB Biopython	Cock et al, 2009	v1.83
FIJI/ImageJ	NIH	2.1.0/1.53c
Compass for SW	Bio-Techne	v7.0.0
GraphPad Prism	GraphPad	V10.2.3
Other		
Ultimate 3000 RSLC	Thermo Fisher Scientific	
Q Exactive Plus	Thermo Fisher Scientific	
JESS Capillary Western	Bio-Techne	

Cloning and generation of the stable miniTurbo-LRRK2 cell line

For comparability, all BioID tags used in this study were generated using an identical cloning strategy, incorporating an N-terminal HA tag for detection and a 3×(GGGS) linker between the tag and the protein of interest, inserted C-terminally via Gateway cloning. The constructs were ordered as synthetic genes (Eurofins) and subcloned via *Eco*RI and *Xho*I into pcDNA3.0 (Invitrogen), allowing the expression of fusion proteins in mammalian cells under the strong viral CMV promoter. Gateway Destination clones were generated by cloning a Gateway cassette (Invitrogen) into an *Eco*RV site at the 3' end and in frame of the different BioID-tags [BioID (Roux et al, 2012; referred as BioID1), BioID2 (Kim et al, 2016), miniTurbo (Branon et al, 2018)]. For better and comparable detection of the fusion proteins, all tags contain an N-terminal HA-tag. The LRRK2 expression clones were subsequently generated by LR cloning (Invitrogen) based on ENTRY clones described earlier (Gloeckner et al, 2010). The CDS of human RAB29 was ordered as a synthetic gene strand (Eurofins) with flanking attB sites to allow its direct cloning into pDONR201 by BP cloning and subsequently cloned into an in-house (N)FLAG-HA Gateway destination clone by the LR reaction. The HEK293 cell line (ACC-305) stably expressing miniTurbo-LRRK2 was generated as previously described (Gloeckner et al, 2007). Briefly, single colonies have been selected and tested after transient transfection and selection via G418 (Sigma). The Flag-HA-CYLD vector was kindly provided by Wade Harper (plasmid #22544, Addgene) (Sowa et al, 2009), the pCMV poly HA-Ubiquitin construct was kindly provided by D. Bohmann (Treier et al, 1994), and the pRK5-HA-Ubiquitin-K63 vector was kindly provided by T. Dawson (plasmid #17606, Addgene) (Lim et al, 2005).

Cell culture and proximity labeling

HEK293T (ACC-635) or HEK293 cells stably expressing miniTurbo-LRRK2 were cultured in 14 cm dishes in Dulbecco's modified Eagle medium (DMEM) supplemented with penicillin–streptomycin and, unless otherwise stated, 10% FBS at 37 °C and 5% CO2. Cells were grown for 8 h to 24 h to reach 50–80% confluency prior to transfection with a self-prepared polyethylenimine (PEI) reagent (Guaitoli et al, 2016). For each condition, 4–6 plates were used. If not stated otherwise, for biotinylation, cells have been incubated with 50 µM biotin (Sigma) in serum-free medium for up to 16 h. In case of the mini turbo tag, cells have been incubated with 50 µM biotin for 2 h after o/n starvation. Starvation was used to synchronize the cells and, in light of the physiological functions of LRRK2, to enrich for post-mitotic states in which its centrosomal and ciliary roles are more prominent. For the determination of the LRRK2-inhibitor dependent proximity proteomes, a HEK293 line stably expressing mT-LRRK2 was either incubated with 1 µM MLi-2, 1 µM GZD-824 or DMSO (vehicle) 1 h prior to and during 2 h biotin incubation. For the analysis of RAB29-dependent proximity proteomes, mT-LRRK2 was either co-expressed with HA-RAB29 or an empty pcDNA3.0 vector. See also the point-to-point protocol deposited on Zenodo (https://doi.org/10.5281/zenodo.17045153).

Affinity purification of biotinylated proteins

For cell lysis, cell culture dishes were transferred to ice, and culture medium was removed. The cells were rinsed two times with 5 ml ice-cold PBS. The cells were covered with 1 ml lysis buffer [1% Nonidet P-40 Substitute (Merck), protease inhibitor cocktail (Roche), PhosSTOP (Roche) in TBS (30 mM Tris-HCl, pH 7.4, and 150 mM NaCl)] per 14 cm dish and detached with a cell scraper. The cell suspension was collected and incubated for 20–40 min on an end-over-end shaker at 4 °C. Lysates were cleared by centrifugation (15,000 × *g* for 10 min at 4 °C). The protein concentration of cleared lysates was determined photometrically using a nanodrop (Thermo-Fisher Scientific) or with the BCA assay (Thermo-Fisher Scientific) following the manufacturer's instructions. Biotinylated proteins were purified by affinity enrichment using either Strep-Tactin Superflow resin (IBA) or MagStrep Strep-Tactin beads (IBA) in case of small-scale enrichments. To this end, the combined lysates for each condition were incubated with an adjusted resin volume of 25 µl packed beads per 14-cm cell culture

dish. The resin was equilibrated by washing 3–4 times with 500 µl lysis buffer. The lysates were incubated with the resin overnight at 4 °C under constant agitation. After incubation, the resin was sedimented by centrifugation at 1000 × *g* for 3 min at 4 °C. The supernatant was removed, leaving ~300 µl to resuspend the resin. The resin suspension was transferred to microSpin columns (Cytiva) and washed three times with 500 µl lysis buffer, followed by two washes with 500 µl 1x TBS (centrifugation for 5 s at 100 × *g*). Biotinylated proteins were eluted by incubation with 300–400 µl desthiobiotin elution buffer (2.5 M, IBA). The desthiobiotin eluates were precipitated by chloroform/methanol and directly subjected to tryptic proteolysis following standard protocols (Gloeckner et al, 2009) and stored at −80 °C. The BioID protocol was further optimized during the course of the study. A detailed step-by-step protocol has been deposited on Zenodo (https://doi.org/10.5281/zenodo.17045153). This protocol includes an additional SDS extraction step after cell lysis and removal of nuclei, and was used in particular for the inhibitor study.

CYLD co-expression experiment

For the analysis of CYLD co-expression, cells were co-transfected with either Strep/FLAG (SF-TAP)-tagged LRRK2 WT or LRRK2 Y1699C together with CYLD. As a negative control, CYLD plasmid was replaced by pCDNA3 empty vector, to maintain the plasmid concentration constant among the different conditions. To test the influence of defined ubiquitin linkage types, ubiquitin—either in WT form (pCMV poly HA-Ubiquitin) or K63 (pRK5-HA-Ubiquitin-K63)—was co-expressed. For experiments relying on endogenous ubiquitin, the ubiquitin expression plasmids were replaced by the pcDNA3 vector. The experiment was performed in 10 cm culture dishes. Cells were seeded at a density of 3 to 4 million cells per dish and transfected the next day using home-made PEI transfection reagent (cell confluency 30-40%). A total of 3.2 µg of plasmid DNA was used for each plate. The plasmid ratios were LRRK2:CYLD:Ubiquitin 1:3:1. Cells were lysed 48 h post-transfection (cell confluency approx. 80%) in 500 µl lysis buffer (see above) and incubated for 45 min at 4 °C under agitation. Cell debris was removed by centrifugation at 1000 × *g* for 10 min at 4 °C. To extract membrane-bound prenylated proteins (e.g., Rab proteins), pre-cleared lysates were supplemented with SDS (55 µl of a 10% stock solution) to a final concentration of 1% and incubated for 15 min at 4 °C under agitation. Lysates were subsequently clarified by centrifugation at 20,000 × *g* for 10 min at room temperature. Protein concentration was determined by BCA assay (Pierce), and LRRK2 levels were assessed by capillary Western blotting (see below).

siRNA knockdown

Twenty-four hours after splitting, cells were transfected with RNAiMAX (Life Technologies) following the manufacturer's instructions. The following siRNAs were used (Silencer Select®, Life Technologies): PCM1 (#s10128, CAAAGACUCCACAUAC-GUUtt), Negative Control No. 2 (#4390846). 360 pmol of siRNA were used for each technical replicate. Cells were kept in culture for another 48 h before proceeding with treatment with 10 µM MLi-2 or DMSO. Cells were lysed as described above. Three technical replicates for each condition (PCM1 or scrambled, MLi-2 or DMSO) were used. The effects of PCM1 knockdown were evaluated via SDS-PAGE and western blot.

SDS PAGE and western blots

For functional evaluation of the bait proteins and to determine the biotinylation efficiency, samples were subjected to SDS PAGE and analyzed by western blotting on PVDF membranes. To assess blotting efficiency and equal loading, the membranes were stained with Ponceau S. Prior to blocking of the membranes in 5% nonfat dry milk powder (BioRad) or 1–5% BSA (Carl Roth) in TBS with 0.1% Tween 20 (TBST) for 1–3 h at RT, membranes were de-stained in TBST. Membranes were afterward incubated with primary antibody solutions overnight at 4 °C under mild agitation. The following primary antibodies were used: rat α-LRRK2 mAb (24D8 clone, hybridoma supernatant, generated in-house (Carrion et al, 2017)) 1:1000 in 5% milk in TBST), rabbit α-pS935-LRRK2 mAb (Abcam, ab133450; 1:100,000 in 5% BSA in TBST), rabbit α-RAB10 mAb (Abcam, ab181367; 1:5000 in 5% milk in TBST), rabbit α-pT73-RAB10 mAb (Abcam, ab230261; 1:1000 in 5% BSA in TBST), rat α-HA-tag (Roche, 3F10 clone, Rat 1gG1; 1:1000 in 5% milk in TBST), mouse α-FLAG-tag (Sigma, F1804-200UG, 1:2000 in 5% milk in TBST), rabbit α-PCM1 (Proteintech, 19856-1-AP, 1:24,000 in 5% milk in TBST), mouse α-CYLD (Proteintech, 66858-1-Ig, 1:1500 in 5% milk in TBST), rabbit α-SSX2IP (Thermo Fisher Scientific, PA5-31495, 1:1000 in 5% milk in TBST). Membranes were washed 5× 5 min in TBST prior to incubation with the HRP-conjugated secondary antibodies α-rat (Jackson Immuno-Research, 112-036-062; 1:7500), α-rabbit (Jackson Immuno-Research, 111-036-045; 1:7500), and α-mouse (Jackson Immuno-Research, 115-036-062; 1:7500), respectively. For the detection of biotinylated proteins, membranes were incubated with Pierce™ High Sensitivity Streptavidin-HRP (Thermo Fisher Scientific, 1:20,000 in 1% BSA in TBST) overnight at 4 °C and washed the next day 5× 5 min in TBST. Blots were developed with Pierce ECL Plus Western Blotting Substrate following the manufacturer's protocol (Thermo Fisher Scientific) and exposed to Amersham Hyperfilm™ ECL (Cytiva). For quantification of LRRK2 in the presence of CYLD, the JESS capillary Western system (Biotechne) was used. Separation was performed on a 25-capillary array (12-230 kDa Fluorescence Separation; SM-FL004-1). LRRK2 was detected by 24D8; 1:25/rabbit anti-rat DyLight-633; 1:50 (Biotechne NBP1-76225) in milk diluent. b-actin was detected by anti-b-actin; 1:500 (R&D Systems MAB8929)/anti-mouse-NIR (Biotechne 043-821); 1:20; in milk diluent. Detection for both proteins was done in the NIR channel. Data analysis was performed using vendor software (Compass for SW, v7.1.0) and custom Python scripts; graphical representations were generated with the Python library Seaborn. Unpaired two-tailed *t* tests were used to compare LRRK2 levels normalized by β-actin.

Mass spectrometry

In solution, proteolysis was performed as previously described (Gloeckner et al, 2009). Briefly, chloroform/methanol precipitates were dissolved in 50 mM ammonium bicarbonate pH 8.0. Cysteines were reduced and alkylated by treatment with 100 mM DTT and 300 mM Iodoacetamide, respectively, following the incubation with trypsin (Sigma-Aldrich) overnight at 37 °C. Samples were desalted by micropipette C-18 solid-phase extraction tips (StageTip, Thermo Fisher Scientific) prior to LC-MSMS analysis. Peptides were subsequently analyzed by LC-MSMS using a nanoflow HPLC system (Ultimate 3000 RSLC; Thermo-Fisher Scientific) coupled to an Orbitrap Q-Exactive plus (Thermo Fisher Scientific) tandem mass spectrometer. Peptides were separated by reversed C-18

chromatography and 120-minute gradients. MS1 spectra were acquired in the Orbitrap at 70 K resolution. After selection of the 10 most intense precursor ions from the MS1 scans for HCD fragmentation (Top 10 method), MS2 spectra were acquired at 17.5 K. RAW MS files were analyzed with Maxquant (version 2.0.3.1), enabling label-free quantification (LFQ with no normalization) and "match between runs" (Cox et al, 2014). For the embedded Andromeda search engine, trypsin has been selected as the enzyme, and carbamylation was set as a fixed modification; N-terminal acetylation was set as a variable modification. The search was performed against the human subset of the Uniprot/Swissprot database (release 2021_04, 20375 entries). The MaxQuant output was further processed by Perseus and SaintExpress.

Perseus post-processing

For post-analysis, the protein groups were further processed by Perseus (v. 1.6.7). LFQ intensities of the individual runs were assigned to their respective conditions, and potential contaminants, reverse hits, as well as proteins identified only by site were filtered out. For further analysis, only IDs with a maximum number of missing values of n-1 in at least one condition were considered. Remaining missing values were replaced by group-wise imputation based on a normal distribution (log2 values) around the detection limit (width=0.3; down-shift=1.8). Intensities of the individual experiments were normalized by their medians, and significantly enriched proteins (condition vs control) were determined by a moderated permutation-based T test (FDR = 0.05, S0 = 0.1) as implemented in Perseus (two-sample test).

SaintExpress post-processing

We followed a previously described protocol (Liu et al, 2020; see also http://proteomics.fi) to select the most confident interactors using the statistical framework of SAINTExpress (Teo et al, 2014), as well as a reference knowledgebase for contaminants (i.e., CRAPome (Mellacheruvu et al, 2013)), to filter out most likely false negative interactors. In particular, we generated the "Bait", "Prey" and "Interaction" files to be subjected to the analysis pipeline from the MaxQuant "*proteinGroups.txt*" file by employing the following columns: "Bait" file (IP name = EV_* or LRRK2_*, bait name = LRRK2, indicator for test and negative control= C = EV_*, T = LRRK2_*); "Interaction" file (IP name = EV_*/LRRK_*, bait name = LRRK2, prey name = interaction partner gene symbol, spectral count or intensity values = LFQ intensity); "Prey" file (prey (protein)name = interaction partner Uniprot accession, prey protein length = Sequence length, prey gene name = gene symbol). The proteins that were not classified through the CRAPome filter were retained together with those passing the filter.

We unified the interactor list from the three BioID experiments. Finally, we retained a list of 208 interactors that passed the two filters. Only 45 proteins in the filtered interactor list are already present in IntAct.

Graphical representation and network annotation

PPI networks were analyzed by Cytoscape version 3.8.2 (Shannon et al, 2003) and were mapped to available interactions from IntAct using the Cytoscape IntAct app (Ragueneau et al, 2021). Networks were annotated with STRINGDB terms via the 'Stringify' function of the StringApp (Doncheva et al, 2019), and functional enrichment was retrieved via the same app. We annotated the networks with the AutoAnnotate plug-in (Kucera et al, 2016), using the GLay clustering method, and generated the cluster labels with the Adjacent Words option of the WordCloud algorithm, based on significantly enriched GO Biological Process and Cellular Component terms associated with the genes in each network. The Venn diagram shown in Fig. 1A has been generated with JVenn provided by the ProteoRE server (Galaxy Version 2021.05.12) (Galaxy, 2024).

Co-evolution-based PPI stratification

Co-evolution of two proteins A and B was measured as the Jaccard similarity coefficient of the set of genomes containing an orthologous sequence of A and the set of genomes containing an orthologous sequence of B. Orthologous sequences were collected from the Orthologous MAtrix (OMA) database (Altenhoff et al, 2021) using a Python script written in-house using the PyOMADB client (Kaleb et al, 2019) (Kaleb et al, 2019) (December 13, 2023, database version July 2023).

AF-multimer prediction of binary interactions

We used Alphafold-Multimer v2.3.2 (preprint: Evans et al, 2021) to generate 3D models of full-length LRRK2 binary interaction complexes for all the interactors shorter than 2000 residues. The databases required to run AlphaFold-Multimer were downloaded on January 12, 2023 and the predictions were run with the flag –max template date = 01-01-1900, to avoid the usage of any available experimental templates. Among the 5 models generated for each LRRK2 binary complex, only the best one was considered for further analysis. The score used to evaluate the models was the default one used by AlphaFold-Multimer (0.2*pTM + 0.8*ipTM).

Interaction fingerprint

AlphaFold produces probabilities for the $C_ß$-$C_ß$ distances between residues i and j to fall into a series of distance bins. For each pair of residues, we calculated the expected value of such distance distribution, yielding a matrix of dimension l_{LRRK2} x l_n, corresponding to the sequence lengths of LRRK2 and the nth interacting partner, respectively. Subsequently, we pooled the distogram on the interaction partner's side and assigned to each residue of LRRK2 the minimum expected distance to any residue of the interactor. We refer to this vector of minimum expected distances as the interaction fingerprint of a given interacting protein.

RMSD calculation

We compared LRRK2 conformations by performing Root Mean Square Deviation (RMSD)-based clustering. To calculate the RMSD we fitted the structures using the C_α atoms of the LRRK2 chains from position 983 to the end of the sequence. The N-terminal portion of the protein was excluded because it is very flexible. Calculations were performed using the Superimposer function of the PDB Biopython module (Cock et al, 2009) (version 1.83) through customized scripts and pipeline (Matic et al, 2023).

Clustering

The clustering was performed using the Ward method with the *clustermap* function from the *seaborn* Python library (version 0.11.2). Results were displayed through matplotlib (https://matplotlib.org/) and seaborn (https://seaborn.pydata.org/) libraries using customized Python scripts. The number of clusters chosen was one that maximized the mean Silhouette Coefficient of all samples (Rousseeuw, 1987), as computed by the *silhouette_score* function in *scikit-learn* (Pedregosa et al, 2011).

Data availability

The mass spectrometry proteomics data have been deposited to the ProteomeXchange Consortium via the PRIDE (Perez-Riverol et al, 2022) partner repository with the dataset identifier PXD048832 and https://doi.org/10.6019/PXD048832 (BioID1, BioID2, miniTurbo), PXD048806 and https://doi.org/10.6019/PXD048806 (LRRK2 proximity-proteomes MLi-2 vs. GZD-524) as well as PXD048808 and https://doi.org/10.6019/PXD048808 (RAB29 co-expression). The BioID interaction network and associated co-evolutionary and structural analysis can be accessed at the following URL: https://dip.bioinfolab.sns.it/explore/. The code used for the analysis is available at the following links: https://github.com/raimondilab/distogram_analysis, https://github.com/raimondilab/Stable_complex_predictor. A point-to-point protocol for the BioID approach was deposited on Zenodo (https://doi.org/10.5281/zenodo.17045153).

The source data of this paper are collected in the following database record: biostudies:S-SCDT-10_1038-S44319-026-00806-4.

Expanded view data, supplementary information, appendices are available for this paper at https://doi.org/10.1038/s44319-026-00806-4.

Peer review information

A peer review file is available at https://doi.org/10.1038/s44319-026-00806-4

References

Almawi AW, Matthews LA, Guarne A (2017) FHA domains: phosphopeptide binding and beyond. Prog Biophys Mol Biol 127:105–110

Altenhoff AM, Train CM, Gilbert KJ, Mediratta I, Mendes de Farias T, Moi D, Nevers Y, Radoykova HS, Rossier V, Warwick Vesztrocy A et al (2021) OMA orthology in 2021: website overhaul, conserved isoforms, ancestral gene order and more. Nucleic Acids Res 49:D373–D379

Bang Y, Kim KS, Seol W, Choi HJ (2016) LRRK2 interferes with aggresome formation for autophagic clearance. Mol Cell Neurosci 75:71–80

Barenz F, Inoue D, Yokoyama H, Tegha-Dunghu J, Freiss S, Draeger S, Mayilo D, Cado I, Merker S, Klinger M et al (2013) The centriolar satellite protein SSX2IP promotes centrosome maturation. J Cell Biol 202:81–95

Beilina A, Rudenko IN, Kaganovich A, Civiero L, Chau H, Kalia SK, Kalia LV, Lobbestael E, Chia R, Ndukwe K et al (2014) Unbiased screen for interactors of leucine-rich repeat kinase 2 supports a common pathway for sporadic and familial Parkinson disease. Proc Natl Acad Sci USA 111:2626–2631

Bersuker K, Peterson CWH, To M, Sahl SJ, Savikhin V, Grossman EA, Nomura DK, Olzmann JA (2018) A proximity labeling strategy provides insights into the composition and dynamics of lipid droplet proteomes. Dev Cell 44:97–112.e117

Boecker CA, Holzbaur ELF (2021) Hyperactive LRRK2 kinase impairs the trafficking of axonal autophagosomes. Autophagy 17:2043–2045

Boldt K, van Reeuwijk J, Lu Q, Koutroumpas K, Nguyen TM, Texier Y, van Beersum SE, Horn N, Willer JR, Mans DA et al (2016) An organelle-specific protein landscape identifies novel diseases and molecular mechanisms. Nat Commun 7:11491

Bonet-Ponce L, Beilina A, Williamson CD, Lindberg E, Kluss JH, Saez-Atienzar S, Landeck N, Kumaran R, Mamais A, Bleck CKE et al (2020) LRRK2 mediates tubulation and vesicle sorting from lysosomes. Sci Adv 6:eabb2454

Branon TC, Bosch JA, Sanchez AD, Udeshi ND, Svinkina T, Carr SA, Feldman JL, Perrimon N, Ting AY (2018) Efficient proximity labeling in living cells and organisms with TurboID. Nat Biotechnol 36:880–887

Carrion MDP, Marsicano S, Daniele F, Marte A, Pischedda F, Di Cairano E, Piovesana E, von Zweydorf F, Kremmer E, Gloeckner CJ et al (2017) The LRRK2 G2385R variant is a partial loss-of-function mutation that affects synaptic vesicle trafficking through altered protein interactions. Sci Rep 7:5377

Chen C, Xu Z, Zhang T, Lin L, Lu M, Xie C, Yu X (2019) Cep85 relays Plk1 activity to phosphorylated Nek2A for its timely activation in centrosome disjunction. iScience 11:114–133

Cock PJ, Antao T, Chang JT, Chapman BA, Cox CJ, Dalke A, Friedberg I, Hamelryck T, Kauff F, Wilczynski B et al (2009) Biopython: freely available Python tools for computational molecular biology and bioinformatics. Bioinformatics 25:1422–1423

Cox J, Hein MY, Luber CA, Paron I, Nagaraj N, Mann M (2014) Accurate proteome-wide label-free quantification by delayed normalization and maximal peptide ratio extraction, termed MaxLFQ. Mol Cell Proteom: MCP 13:2513–2526

Dammermann A, Merdes A (2002) Assembly of centrosomal proteins and microtubule organization depends on PCM-1. J Cell Biol 159:255–266

Deniston CK, Salogiannis J, Mathea S, Snead DM, Lahiri I, Matyszewski M, Donosa O, Watanabe R, Bohning J, Shiau AK et al (2020) Structure of LRRK2 in Parkinson's disease and model for microtubule interaction. Nature 588:344–349

Dhekne HS, Tonelli F, Yeshaw WM, Chiang CY, Limouse C, Jaimon E, Purlyte E, Alessi DR, Pfeffer SR (2023) Genome-wide screen reveals Rab12 GTPase as a critical activator of Parkinson's disease-linked LRRK2 kinase. eLife 12:e87098

Dhekne HS, Yanatori I, Gomez RC, Tonelli F, Diez F, Schule B, Steger M, Alessi DR, Pfeffer SR (2018) A pathway for Parkinson's disease LRRK2 kinase to block primary cilia and Sonic hedgehog signaling in the brain. eLife 7:e40202

Dobson-Stone C, Hallupp M, Shahheydari H, Ragagnin AMG, Chatterton Z, Carew-Jones F, Shepherd CE, Stefen H, Paric E, Fath T et al (2020) CYLD is a causative gene for frontotemporal dementia-amyotrophic lateral sclerosis. Brain 143:783–799

Doncheva NT, Morris JH, Gorodkin J, Jensen LJ (2019) Cytoscape StringApp: network analysis and visualization of proteomics data. J Proteome Res 18:623–632

Douanne T, Andre-Gregoire G, Thys A, Trillet K, Gavard J, Bidere N (2019) CYLD regulates centriolar satellites proteostasis by counteracting the E3 ligase MIB1. Cell Rep 27:1657–1665.e1654

Eguether T, Ermolaeva MA, Zhao Y, Bonnet MC, Jain A, Pasparakis M, Courtois G, Tassin AM (2014) The deubiquitinating enzyme CYLD controls apical docking of basal bodies in ciliated epithelial cells. Nat Commun 5:4585

Ehebauer MT, Arias AM (2009) The structural and functional determinants of the Axin and Dishevelled DIX domains. BMC Struct Biol 9:70

Evans R, O'Neill M, Pritzel A, Antropova N, Senior A, Green T, Žídek A, Bates R, Blackwell S, Yim J et al (2021) Protein complex prediction with AlphaFold-Multimer. Preprint at bioRxiv https://doi.org/10.1101/2021.10.04.463034

Fahn S (2003) Description of Parkinson's disease as a clinical syndrome. Ann N Y Acad Sci 991:1–14

Filippini F, Nola S, Zahraoui A, Roger K, Esmaili M, Sun J, Wojnacki J, Vlieghe A, Bun P, Blanchon S et al (2023) Secretion of VGF relies on the interplay between LRRK2 and post-Golgi v-SNAREs. Cell Rep 42:112221

Follett J, Farrer MJ (2021) LRRK2; a dynamic regulator of cellular trafficking. Brain Res 1761:147394

Galaxy C (2024) The Galaxy platform for accessible, reproducible, and collaborative data analyses: 2024 update. Nucleic Acids Res 52:W83–W94

Gasser T, Hardy J, Mizuno Y (2011) Milestones in PD genetics. Mov Disord 26:1042–1048

Geisler S, Holmstrom KM, Skujat D, Fiesel FC, Rothfuss OC, Kahle PJ, Springer W (2010) PINK1/Parkin-mediated mitophagy is dependent on VDAC1 and p62/SQSTM1. Nat Cell Biol 12:119–131

Gloeckner CJ, Boldt K, Schumacher A, Roepman R, Ueffing M (2007) A novel tandem affinity purification strategy for the efficient isolation and characterisation of native protein complexes. Proteomics 7:4228–4234

Gloeckner CJ, Boldt K, Ueffing M (2009) Strep/FLAG tandem affinity purification (SF-TAP) to study protein interactions. Curr Protoc Protein Sci. https://doi.org/10.1002/0471140864.ps1920s57

Gloeckner CJ, Boldt K, von Zweydorf F, Helm S, Wiesent L, Sarioglu H, Ueffing M (2010) Phosphopeptide analysis reveals two discrete clusters of phosphorylation in the N-terminus and the Roc domain of the Parkinson-disease associated protein kinase LRRK2. J Proteome Res 9:1738–1745

Gloeckner CJ, Porras P (2020) Guilt-by-association—functional insights gained from studying the LRRK2 interactome. Front Neurosci 14:485

Grishin NV (2001) KH domain: one motif, two folds. Nucleic Acids Res 29:638–643

Guaitoli G, Raimondi F, Gilsbach BK, Gomez-Llorente Y, Deyaert E, Renzi F, Li X, Schaffner A, Jagtap PK, Boldt K et al (2016) Structural model of the dimeric Parkinson's protein LRRK2 reveals a compact architecture involving distant interdomain contacts. Proc Natl Acad Sci USA 113:E4357–4366

Guaitoli G, Zhang X, Saitta F, Miglionico P, Silbermann LM, Ho FY, von Zweydorf F, Signorelli M, Tych K, Fessas D et al (2023) Biophysical analysis reveals autophosphorylation as an important regulator of LRRK2 dimerization. Preprint at bioRxiv https://doi.org/10.1101/2023.08.11.549911

Hall EA, Kumar D, Prosser SL, Yeyati PL, Herranz-Perez V, Garcia-Verdugo JM, Rose L, McKie L, Dodd DO, Tennant PA et al (2023) Centriolar satellites expedite mother centriole remodeling to promote ciliogenesis. eLife 12:e79299

Hallett PJ, Engelender S, Isacson O (2019) Lipid and immune abnormalities causing age-dependent neurodegeneration and Parkinson's disease. J Neuroinflammation 16:153

Hori A, Toda T (2017) Regulation of centriolar satellite integrity and its physiology. Cell Mol Life Sci: CMLS 74:213–229

Islam MS, Nolte H, Jacob W, Ziegler AB, Putz S, Grosjean Y, Szczepanowska K, Trifunovic A, Braun T, Heumann H et al (2016) Human R1441C LRRK2 regulates the synaptic vesicle proteome and phosphoproteome in a Drosophila model of Parkinson's disease. Hum Mol Genet 25:5365–5382

Jennings D, Huntwork-Rodriguez S, Henry AG, Sasaki JC, Meisner R, Diaz D, Solanoy H, Wang X, Negrou E, Bondar VV et al (2022) Preclinical and clinical evaluation of the LRRK2 inhibitor DNL201 for Parkinson's disease. Sci Transl Med 14:eabj2658

Jian F, Wang S, Tian R, Wang Y, Li C, Li Y, Wang S, Fang C, Ma C, Rong Y (2024) The STX17-SNAP47-VAMP7/VAMP8 complex is the default SNARE complex mediating autophagosome-lysosome fusion. Cell Res 34:151–168

Kafka A, Basic-Kinda S, Pecina-Slaus N (2014) The cellular story of dishevelleds. Croat Med J 55:459–467

Kaleb K, Vesztrocy AW, Altenhoff A, Dessimoz C (2019) Expanding the Orthologous Matrix (OMA) programmatic interfaces: REST API and the OmaDB packages for R and Python. F1000Res 8:42

Kalogeropulou AF, Purlyte E, Tonelli F, Lange SM, Wightman M, Prescott AR, Padmanabhan S, Sammler E, Alessi DR (2022) Impact of 100 LRRK2 variants linked to Parkinson's Disease on kinase activity and microtubule binding. Biochem J 479:1759–1783

Kalogeropulou AF, Zhao J, Bolliger MF, Memou A, Narasimha S, Molitor TP, Wilson WH, Rideout HJ, Nichols RJ (2018) P62/SQSTM1 is a novel leucine-rich repeat kinase 2 (LRRK2) substrate that enhances neuronal toxicity. Biochem J 475:1271–1293

Kanao T, Venderova K, Park DS, Unterman T, Lu B, Imai Y (2010) Activation of FoxO by LRRK2 induces expression of proapoptotic proteins and alters survival of postmitotic dopaminergic neuron in Drosophila. Hum Mol Genet 19:3747–3758

Khan SS, Jaimon E, Lin YE, Nikoloff J, Tonelli F, Alessi DR, Pfeffer SR (2024) Loss of primary cilia and dopaminergic neuroprotection in pathogenic LRRK2-driven and idiopathic Parkinson's disease. Proc Natl Acad Sci USA 121:e2402206121

Kim DI, Jensen SC, Noble KA, Kc B, Roux KH, Motamedchaboki K, Roux KJ (2016) An improved smaller biotin ligase for BioID proximity labeling. Mol Biol Cell 27:1188–1196

Kluss JH, Bonet-Ponce L, Lewis PA, Cookson MR (2022a) Directing LRRK2 to membranes of the endolysosomal pathway triggers RAB phosphorylation and JIP4 recruitment. Neurobiol Dis 170:105769

Kluss JH, Lewis PA, Greggio E (2022b) Leucine-rich repeat kinase 2 (LRRK2): an update on the potential therapeutic target for Parkinson's disease. Expert Opin Ther Targets 26:537–546

Kucera M, Isserlin R, Arkhangorodsky A, Bader GD (2016) AutoAnnotate: a Cytoscape app for summarizing networks with semantic annotations. F1000Res 5:1717

Kumar M, Acevedo-Cintron J, Jhaldiyal A, Wang H, Andrabi SA, Eacker S, Karuppagounder SS, Brahmachari S, Chen R, Kim H et al (2020) Defects in mitochondrial biogenesis drive mitochondrial alterations in PARKIN-deficient human dopamine neurons. Stem Cell Rep 15:629–645

Lara Ordonez AJ, Fasiczka R, Fernandez B, Naaldijk Y, Fdez E, Blanca Ramirez M, Phan S, Boassa D, Hilfiker S (2022) The LRRK2 signaling network converges on a centriolar phospho-Rab10/RILPL1 complex to cause deficits in centrosome cohesion and cell polarization. Biol Open 11:bio059468

Lara Ordonez AJ, Fernandez B, Fdez E, Romo-Lozano M, Madero-Perez J, Lobbestael E, Baekelandt V, Aiastui A, Lopez de Munain A, Melrose HL et al (2019) RAB8, RAB10 and RILPL1 contribute to both LRRK2 kinase-mediated centrosomal cohesion and ciliogenesis deficits. Hum Mol Genet 28:3552–3568

Li BJ, Chen H, Jiang SS, Wang CY, Tuo QH, Long SY, Zhang CP, Liao DF (2020) PX domain-containing kinesin KIF16B and microtubule-dependent intracellular movements. J Membr Biol 253:101–108

Li P, Li J, Wang L, Di LJ (2017) Proximity labeling of interacting proteins: application of BioID as a discovery tool. Proteomics. https://doi.org/10.1002/pmic.201700002

Li X, Zhu H, Huang BT, Li X, Kim H, Tan H, Zhang Y, Choi I, Peng J, Xu P et al (2024) RAB12-LRRK2 complex suppresses primary ciliogenesis and regulates centrosome homeostasis in astrocytes. Nat Commun 15:8434

Lim KL, Chew KC, Tan JM, Wang C, Chung KK, Zhang Y, Tanaka Y, Smith W, Engelender S, Ross CA et al (2005) Parkin mediates nonclassical, proteasomal-independent ubiquitination of synphilin-1: implications for Lewy body formation. J Neurosci 25:2002–2009

Liu X, Salokas K, Weldatsadik RG, Gawriyski L, Varjosalo M (2020) Combined proximity labeling and affinity purification-mass spectrometry workflow for mapping and visualizing protein interaction networks. Nat Protoc 15:3182–3211

Lobbestael E, Civiero L, De Wit T, Taymans JM, Greggio E, Baekelandt V (2016) Pharmacological LRRK2 kinase inhibition induces LRRK2 protein destabilization and proteasomal degradation. Sci Rep 6:33897

Manzoni C, Denny P, Lovering RC, Lewis PA (2015) Computational analysis of the LRRK2 interactome. PeerJ 3:e778

Matic M, Miglionico P, Tatsumi M, Inoue A, Raimondi F (2023) GPCRome-wide analysis of G-protein-coupling diversity using a computational biology approach. Nat Commun 14:4361

McGrath E, Waschbusch D, Baker BM, Khan AR (2021) LRRK2 binds to the Rab32 subfamily in a GTP-dependent manner via its armadillo domain. Small GTPases 12:133–146

Meixner A, Boldt K, Van Troys M, Askenazi M, Gloeckner CJ, Bauer M, Marto JA, Ampe C, Kinkl N, Ueffing M (2011) A QUICK screen for Lrrk2 interaction partners—leucine-rich repeat kinase 2 is involved in actin cytoskeleton dynamics. Mol Cell Proteom: MCP 10:M110 001172

Meldal BHM, Perfetto L, Combe C, Lubiana T, Ferreira Cavalcante JV, Bye AJH, Waagmeester A, Del-Toro N, Shrivastava A, Barrera E et al (2022) Complex Portal 2022: new curation frontiers. Nucleic Acids Res 50:D578–D586

Mellacheruvu, Wright D, Couzens AL Z, Lambert JP, St-Denis NA, Li T, Miteva YV, Hauri S, Sardiu ME, Low TY et al (2013) The CRAPome: a contaminant repository for affinity purification-mass spectrometry data. Nat Methods 10:730–736

Miglionico P, Nemati Fard LA, Gloeckner CJ, Raimondi F (2024) Prediction and discovery of protein-protein direct interactions and stable complexes based on gene co-expression and co-evolution. Preprint at bioRxiv https://doi.org/10.1101/2024.10.05.616780

Miller GK, Kuruvilla S, Jacob B, LaFranco-Scheuch L, Bakthavatchalu V, Flor J, Flor K, Ziegler J, Reichard C, Manfre P et al (2023) Effects of LRRK2 inhibitors in nonhuman primates. Toxicol Pathol 51:232–245

Mohd Rafiq N, Fujise K, Rosenfeld MS, Xu P, De Camilli P (2024) Parkinsonism Sac domain mutation in Synaptojanin-1 affects ciliary properties in iPSC-derived dopaminergic neurons. Proc Natl Acad Sci USA 121:e2318943121

Moreira C, Kelemen CD, Obado SO, Zahedifard F, Zhang N, Holetz FB, Gauglitz L, Dallagiovanna B, Field MC, Kramer S et al (2023) Impact of inherent biases built into proteomic techniques: proximity labeling and affinity capture compared. J Biol Chem 299:102726

Myasnikov A, Zhu H, Hixson P, Xie B, Yu K, Pitre A, Peng J, Sun J (2021) Structural analysis of the full-length human LRRK2. Cell 184:3519–3527.e3510

Naaldijk Y, Fernandez B, Fasiczka R, Fdez E, Leghay C, Croitoru I, Kwok JB, Boulesnane Y, Vizeneux A, Mutez E et al (2024) A potential patient stratification biomarker for Parkinson's disease based on LRRK2 kinase-mediated centrosomal alterations in peripheral blood-derived cells. NPJ Parkinsons Dis 10:12

Orchard S, Ammari M, Aranda B, Breuza L, Briganti L, Broackes-Carter F, Campbell NH, Chavali G, Chen C, del-Toro N et al (2014) The MIntAct project—IntAct as a common curation platform for 11 molecular interaction databases. Nucleic Acids Res 42:D358–363

Paisan-Ruiz C, Jain S, Evans EW, Gilks WP, Simon J, van der Brug M, Lopez de Munain A, Aparicio S, Gil AM, Khan N et al (2004) Cloning of the gene containing mutations that cause PARK8-linked Parkinson's disease. Neuron 44:595–600

Park S, Han S, Choi I, Kim B, Park SP, Joe EH, Suh YH (2016) Interplay between leucine-rich repeat kinase 2 (LRRK2) and p62/SQSTM-1 in selective autophagy. PLoS ONE 11:e0163029

Pedregosa F, Varoquaux G, Gramfort A, Michel VBT, Griesel O, Blondel M, Prettenhofer P, Weiss R, Dubourg V et al (2011) Scikit-learn: machine learning in Python. J Mach Learn Res 12:2825–2830

Perez-Riverol Y, Bai J, Bandla C, Garcia-Seisdedos D, Hewapathirana S, Kamatchinathan S, Kundu DJ, Prakash A, Frericks-Zipper A, Eisenacher M et al (2022) The PRIDE database resources in 2022: a hub for mass spectrometry-based proteomics evidences. Nucleic Acids Res 50:D543–D552

Piccoli G, Condliffe SB, Bauer M, Giesert F, Boldt K, De Astis S, Meixner A, Sarioglu H, Vogt-Weisenhorn DM, Wurst W et al (2011) LRRK2 controls synaptic vesicle storage and mobilization within the recycling pool. J Neurosci 31:2225–2237

Piccoli G, Onofri F, Cirnaru MD, Kaiser CJ, Jagtap P, Kastenmuller A, Pischedda F, Marte A, von Zweydorf F, Vogt A et al (2014) Leucine-rich repeat kinase 2 binds to neuronal vesicles through protein interactions mediated by its C-terminal WD40 domain. Mol Cell Biol 34:2147–2161

Pirooznia SK, Wang H, Panicker N, Kumar M, Neifert S, Dar MA, Lau E, Kang BG, Redding-Ochoa J, Troncoso JC et al (2022) Deubiquitinase CYLD acts as a negative regulator of dopamine neuron survival in Parkinson's disease. Sci Adv 8:eabh1824

Prosser SL, Tkach J, Gheiratmand L, Kim J, Raught B, Morrison CG, Pelletier L (2022) Aggresome assembly at the centrosome is driven by CP110-CEP97-CEP290 and centriolar satellites. Nat Cell Biol 24:483–496

Purlyte E, Dhekne HS, Sarhan AR, Gomez R, Lis P, Wightman M, Martinez TN, Tonelli F, Pfeffer SR, Alessi DR (2018) Rab29 activation of the Parkinson's disease-associated LRRK2 kinase. EMBO J 37:1–18

Qin W, Cho KF, Cavanagh PE, Ting AY (2021) Deciphering molecular interactions by proximity labeling. Nat Methods 18:133–143

Ragueneau E, Shrivastava A, Morris JH, Del-Toro N, Hermjakob H, Porras P (2021) IntAct App: a Cytoscape application for molecular interaction network visualization and analysis. Bioinformatics 37:3684–3685

Raig ND, Surridge KJ, Sanz-Murillo M, Dederer V, Kramer A, Schwalm MP, Lattal NM, Elson L, Chatterjee D, Mathea S et al (2025) Type II kinase inhibitors that target Parkinson's disease-associated LRRK2. Sci Adv 11:eadt2050

Rousseeuw PJ (1987) Silhouettes: a graphical aid to the interpretation and validation of cluster analysis. J Comput Appl Math 20:53–65

Roux KJ, Kim DI, Raida M, Burke B (2012) A promiscuous biotin ligase fusion protein identifies proximal and interacting proteins in mammalian cells. J Cell Biol 196:801–810

Sancho RM, Law BM, Harvey K (2009) Mutations in the LRRK2 Roc-COR tandem domain link Parkinson's disease to Wnt signalling pathways. Hum Mol Genet 18:3955–3968

Schmidt S, Luecken MD, Trumbach D, Hembach S, Niedermeier KM, Wenck N, Pflugler K, Stautner C, Bottcher A, Lickert H et al (2022) Primary cilia and SHH signaling impairments in human and mouse models of Parkinson's disease. Nat Commun 13:4819

Shannon P, Markiel A, Ozier O, Baliga NS, Wang JT, Ramage D, Amin N, Schwikowski B, Ideker T (2003) Cytoscape: a software environment for integrated models of biomolecular interaction networks. Genome Res 13:2498–2504

Shin WH, Park JH, Chung KC (2020) The central regulator p62 between ubiquitin proteasome system and autophagy and its role in the mitophagy and Parkinson's disease. BMB Rep 53:56–63

Simon-Sanchez J, Schulte C, Bras JM, Sharma M, Gibbs JR, Berg D, Paisan-Ruiz C, Lichtner P, Scholz SW, Hernandez DG et al (2009) Genome-wide association study reveals genetic risk underlying Parkinson's disease. Nat Genet 41:1308–1312

Sowa ME, Bennett EJ, Gygi SP, Harper JW (2009) Defining the human deubiquitinating enzyme interaction landscape. Cell 138:389–403

Steger M, Diez F, Dhekne HS, Lis P, Nirujogi RS, Karayel O, Tonelli F, Martinez TN, Lorentzen E, Pfeffer SR et al (2017) Systematic proteomic analysis of LRRK2-mediated Rab GTPase phosphorylation establishes a connection to ciliogenesis. eLife 6:e31012

Stevens DA, Lee Y, Kang HC, Lee BD, Lee YI, Bower A, Jiang H, Kang SU, Andrabi SA, Dawson VL et al (2015) Parkin loss leads to PARIS-dependent declines in mitochondrial mass and respiration. Proc Natl Acad Sci USA 112:11696–11701

Tasegian A, Singh F, Ganley IG, Reith AD, Alessi DR (2021) Impact of Type II LRRK2 inhibitors on signaling and mitophagy. Biochem J 478:3555–3573

Taylor SS, Kaila-Sharma P, Weng JH, Aoto P, Schmidt SH, Knapp S, Mathea S, Herberg FW (2020) Kinase domain is a dynamic hub for driving LRRK2 allostery. Front Mol Neurosci 13:538219

Teo G, Liu G, Zhang J, Nesvizhskii AI, Gingras AC, Choi H (2014) SAINTexpress: improvements and additional features in significance analysis of INTeractome software. J Proteom 100:37–43

Tollenaere MAX, Villumsen BH, Blasius M, Nielsen JC, Wagner SA, Bartek J, Beli P, Mailand N, Bekker-Jensen S (2015) p38- and MK2-dependent signalling promotes stress-induced centriolar satellite remodelling via 14-3-3-dependent sequestration of CEP131/AZI1. Nat Commun 6:10075

Treier M, Staszewski LM, Bohmann D (1994) Ubiquitin-dependent c-Jun degradation in vivo is mediated by the delta domain. Cell 78:787–798

Tyanova S, Temu T, Sinitcyn P, Carlson A, Hein MY, Geiger T, Mann M, Cox J (2016) The Perseus computational platform for comprehensive analysis of (prote)omics data. Nat Methods 13:731–740

Vides EG, Adhikari A, Chiang CY, Lis P, Purlyte E, Limouse C, Shumate JL, Spinola-Lasso E, Dhekne HS, Alessi DR et al (2022) A feed-forward pathway drives LRRK2 kinase membrane recruitment and activation. eLife 11:e79771

Waschbusch D, Michels H, Strassheim S, Ossendorf E, Kessler D, Gloeckner CJ, Barnekow A (2014) LRRK2 transport is regulated by its novel interacting partner Rab32. PLoS ONE 9:e111632

Wauters L, Versees W, Kortholt A (2019) Roco proteins: GTPases with a baroque structure and mechanism. Int J Mol Sci 20:147

Wilhelm LP, Zapata-Munoz J, Villarejo-Zori B, Pellegrin S, Freire CM, Toye AM, Boya P, Ganley IG (2022) BNIP3L/NIX regulates both mitophagy and pexophagy. EMBO J 41:e111115

Xue J, Zhang J, Zhang J, Liu J, Wang F, Li K, Liu C (2023) The Parkinson's disease-associated mutation LRRK2 G2385R alters mitochondrial biogenesis via the PGC-1alpha-TFAM pathway. Mitochondrion 73:10–18

Yang Y, Ran J, Liu M, Li D, Li Y, Shi X, Meng D, Pan J, Ou G, Aneja R et al (2014) CYLD mediates ciliogenesis in multiple organs by deubiquitinating Cep70 and inactivating HDAC6. Cell Res 24:1342–1353

Yu M, Arshad M, Wang W, Zhao D, Xu L, Zhou L (2018) LRRK2 mediated Rab8a phosphorylation promotes lipid storage. Lipids Health Dis 17:34

Zhao Y, Bracher-Smith M, Li Y, Harvey K, Escott-Price V, Lewis PA, Manzoni C (2024) Transcriptomics and weighted protein network analyses of the LRRK2 protein interactome reveal distinct molecular signatures for sporadic and LRRK2 Parkinson's disease. NPJ Parkinsons Dis 10:144

Zhao Y, Vavouraki N, Lovering RC, Escott-Price V, Harvey K, Lewis PA, Manzoni C (2023) Tissue specific LRRK2 interactomes reveal a distinct striatal functional unit. PLoS Comput Biol 19:e1010847

Zheng L, Bernard-Marissal N, Moullan N, D'Amico D, Auwerx J, Moore DJ, Knott G, Aebischer P, Schneider BL (2017) Parkin functionally interacts with PGC-1α to preserve mitochondria and protect dopaminergic neurons. Hum Mol Genet 26:582–598

Zhu H, Hixson P, Ma W, Sun J (2024) Pharmacology of LRRK2 with type I and II kinase inhibitors revealed by cryo-EM. Cell Discov 10:10

Zhu H, Tonelli F, Turk M, Prescott A, Alessi DR, Sun J (2023) Rab29-dependent asymmetrical activation of leucine-rich repeat kinase 2. Science 382:1404–1411

Zimprich A, Biskup S, Leitner P, Lichtner P, Farrer M, Lincoln S, Kachergus J, Hulihan M, Uitti RJ, Calne DB et al (2004) Mutations in LRRK2 cause autosomal-dominant Parkinsonism with pleomorphic pathology. Neuron 44:601–607

Acknowledgements

We are grateful to the staff of the Core Facility for Medical Proteomics at the medical faculty of the University of Tübingen for technical assistance. Furthermore, we gratefully acknowledge the computational resources of the Center for High Performance Computing (CHPC) at SNS. CJG received funds from The Michael J. Fox Foundation for Parkinson's Research (grant ID: MJFF-8068.02, MJFF-8068.04, and MJFF-023920) and iMed – the Helmholtz Initiative on Personalized Medicine.

Author contributions

Marita Eckert: Investigation; Writing—original draft. **Pasquale Miglionico**: Formal analysis; Visualization; Writing—original draft; Writing—review and editing. **Francesca Izzi**: Formal analysis; Validation; Visualization; Writing—review and editing. **Natalia De Oliveira Rosa**: Resources; Formal analysis. **Benjamin Riebenbauer**: Data curation; Formal analysis. **Marius Ueffing**: Resources; Writing—review and editing. **Francesco Raimondi**: Conceptualization; Formal analysis; Supervision; Visualization; Writing—original draft; Writing—review and editing. **Christian Johannes Gloeckner**: Conceptualization; Formal analysis; Supervision; Writing—original draft; Writing—review and editing.

Source data underlying figure panels in this paper may have individual authorship assigned. Where available, figure panel/source data authorship is listed in the following database record: biostudies:S-SCDT-10_1038-S44319-026-00806-4.

Funding

Open Access funding enabled and organized by Projekt DEAL.

Disclosure and competing interests statement

The authors declare no competing interests.

Expanded View Figures

Figure EV1. Interface fingerprint clustering of LRRK2 modulator-dependent binary complexes.

(**A**) interaction fingerprint clustering of LRRK2's modulators (MLi-2 and RAB29) interactomes. Cells contain the minimum expected distance obtained from the distograms of any residue of each interactor (row) to every residue in LRRK2 (column). Rows are color annotated based on confidence score, Jaccard, RMSD from reference LRRK2 structure (PDB: 7LHW), and experiment type (either MLi-2 or RAB29 overexpression). (**B**) Interaction fingerprint of LRRK2 and interacting RABs (from IntAct).

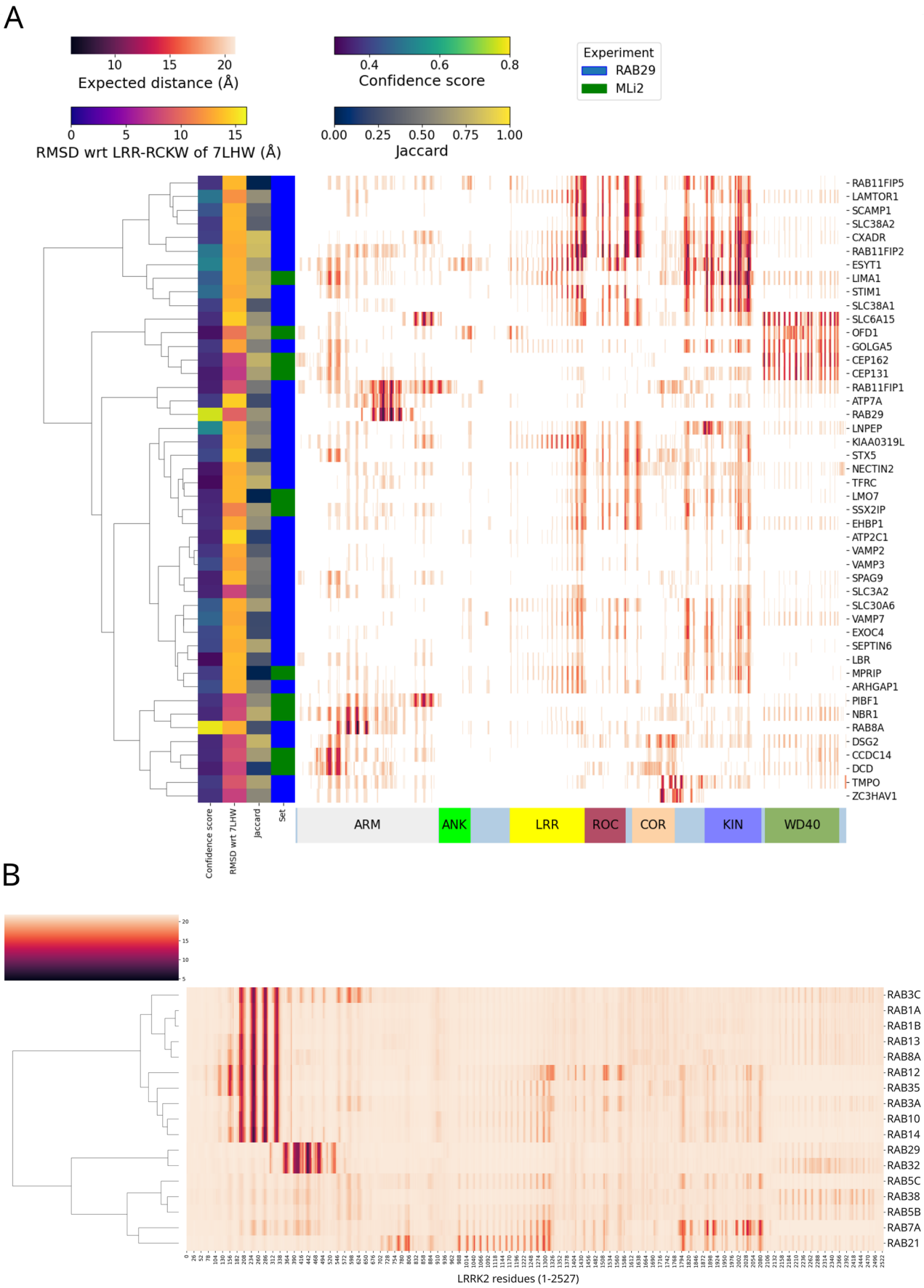
A
Expected distance (Å)
10 15 20
Confidence score
0.4 0.6 0.8
Experiment
RAB29
MLi2
RMSD wrt LRR-RCKW of 7LHW (Å)
0 5 10 15
Jaccard
0.00 0.25 0.50 0.75 1.00
RAB11FIP5
LAMTOR1
SCAMP1
SLC38A2
CXADR
RAB11FIP2
ESYT1
LIMA1
STIM1
SLC38A1
SLC6A15
OFD1
GOLGA5
CEP162
CEP131
RAB11FIP1
ATP7A
RAB29
LNPEP
KIAA0319L
STX5
NECTIN2
TFRC
LMO7
SSX2IP
EHBP1
ATP2C1
VAMP2
VAMP3
SPAG9
SLC3A2
SLC30A6
VAMP7
EXOC4
SEPTIN6
LBR
MPRIP
ARHGAP1
PIBF1
NBR1
RAB8A
DSG2
CCDC14
DCD
TMPO
ZC3HAV1
Confidence score
RMSD wrt 7LHW
Jaccard
Set
ARM
ANK
LRR
ROC
COR
KIN
WD40
B
RAB3C
RAB1A
RAB1B
RAB13
RAB8A
RAB12
RAB35
RAB3A
RAB10
RAB14
RAB29
RAB32
RAB5C
RAB38
RAB5B
RAB7A
RAB21
LRRK2 residues (1-2527)